Tidal mixing events on the deep flanks of Kaena Ridge, Hawaii

JEROME AUCAN, MARK A. MERRIFIELD, DOUGLAS S. LUTHER AND

PIERRE FLAMENT

University of Hawai'i, Department of Oceanography

Submitted, *Journal of Physical Oceanography,* 15 September 2004

Manuscript received in final form 7 September 2005

Corresponding author address:

Jerome Aucan, 1000 Pope Road, Honolulu HI 96822 USA

E-mail : jaucan@soest.hawaii.edu

ABSTRACT

A 3-month mooring deployment (Aug.-Nov. 2002) was made in $2425m$ depth, on the south flank of Kaena Ridge, Hawaii to examine tidal variations within $200m$ of the steeply sloping bottom. Horizontal currents and vertical displacements, inferred from temperature fluctuations, are dominated by the semidiurnal internal tide, with amplitudes of $\geqslant 0.1ms^{-1}$ and $\sim 100m$, respectively. A series of temperature sensors detected tidally-driven overturns with vertical scales of $\sim 100m$. A Thorpe scale analysis of the overturns yields a time-averaged dissipation near the bottom of $1.2 \times 10^{-8}Wkg^{-1}$, 10 to 100 times higher than at similar depths in the ocean interior $50km$ from the Ridge. Dissipation events much larger than the overall mean (up to $10^{-6}Wkg^{-1}$) occur predominantly during two phases of the semidiurnal tide: 1) at peak downslope flows when the tidal stratification is minimum ($N = 5 \times 10^{-4}s^{-1}$), and 2) at the flow reversal from down to upslope flow when the tidal stratification is ordinarily increasing ($N = 10^{-3}s^{-1}$). Dissipation associated with flow reversal mixing is twice that of downslope flow mixing. Although the overturn events occur at these tidal phases and they exhibit a general spring-neap modulation, they are not as regular as the tidal currents. Shear instabilities, particularly due to tidal strain enhancements, appear to trigger downslope flow mixing. Convective instabilities are proposed as the cause for flow reversal mixing, owing to the oblique propagation of the internal tidal down the slope. The generation of similar tidally-driven mixing features on continental slopes has been attributed to oblique wave propagation in previous studies. Because the mechanical energy source for mixing is primarily due to the internal tide rather than the surface tide, the observed intermittency of overturn events is attributed to the broad-banded nature of the internal tide.

1. Introduction

Deep ocean diapycnal mixing is an important but poorly understood component of the general ocean circulation. One common viewpoint of the thermohaline circulation is that dense water sinks at high latitudes, spreads throughout the ocean interior, and returns to the surface in regions of upwelling. Munk (1966) speculated that this upward advection of cold water is balanced by a mechanically driven downward diffusion of heat, resulting in the observed stratification below the main thermocline. The amount of diapycnal mixing necessary to maintain abyssal stratification was estimated by Munk (1966) and later by Munk and Wunsch (1998) to be equivalent to a global-averaged eddy diffusivity of $K_\rho = 10^{-4} m^2 s^{-1}$. Decades of direct turbulence measurements in the open ocean have failed to find much more than a tenth of this value (Gregg 1991). But Munk (1966) had also suggested that the required global average might be dominated by intense mixing in localized regions near topography. This idea has been refined with theory and observations, beginning with Armi (1978) and Armi (1979). It is now known that diapycnal mixing below the thermocline is strongly dependent on location, being largest in the vicinity of rough seafloor topography (Kunze and Toole 1997; Toole et al. 1997; Polzin et al. 1997). The locations of the diapycnal mixing may determine the structure of the deep ocean circulation (Samelson 1998; Hasumi and Suginohara 1999; Simmons et al. 2004). It can then be argued that a better knowledge of the spatial and temporal variations of mixing is paramount to a better understanding of the world's ocean circulation and its impact on climate (Rahmstorf 2003).

When turbulent mixing in a stratified layer occurs along a sloping boundary, mixed fluid is exported from the boundary layer to the interior, and undisturbed stratified fluid is incorporated into the boundary layer (Phillips et al. 1986; Garrett 1991). The mixed water, but not the turbulence

itself, can then spread laterally (e.g, via stirring by mesoscale variability) along neutral surfaces into the ocean's interior (Munk and Wunsch 1998). Enhanced mixing can also occur outside the boundary layer, although still within the neighborhood of the boundary, engendered by enhanced shear and strain from internal waves propagating outward from boundary sources. Although less relevant for our study, the reflection of incident internal waves can cause enhanced mixing along near-critical slopes (Eriksen 1998; Nash et al. 2004b).

Mechanical energy can be supplied to deep boundary layers by a variety of processes, including large scale and localized currents (Gross et al. 1986; Lukas et al. 2000) and/or a wide range of interactions between internal waves and topography (see Thorpe (1999) for a review). The challenge is to document the mixing associated with these processes along sloping boundaries, and ultimately to parameterize their effects in circulation models. In this regard, the tide is both an important source of mechanical energy, believed to be comparable to the surface wind stress (Wunsch 2000), and, because of its inherent predictability, a good candidate for parameterization. Recent studies have demonstrated the link between turbulent mixing and tidal processes (New and Pingree (1990), Lien and Gregg (2001) among others). Furthermore, Egbert and Ray (2000) estimate that $25 - 30\%$ of barotropic tidal dissipation occurs in the open ocean, primarily through the generation of internal tides.

It is now well established from various in situ and remote observations that energetic semi-diurnal internal tides originate from the Hawaiian ridge (Ray and Mitchum 1996; Dushaw et al. 1995). The Hawaii Ocean Mixing Experiment (HOME) was designed to investigate the details of the tidal dissipation along the Hawaiian chain. As part of the HOME modeling effort, the Princeton Ocean Model (POM) has been used to simulate barotropic to baroclinic tidal energy conversion at Kaena Ridge in the Kauai Channel (figure 1). The simulations show internal tide

energy originating on each side of the ridge near the crest (Merrifield et al. (2005)). The energy propagates along internal wave characteristics; one beam propagates up and away from the ridge, a second propagates up and over the ridge, and a third propagates downward along the ridge flank when there is either a near- or super-critical slope below the generation site (figure 2). Energy dissipated by this down-going beam as it propagates along the ridge flank is available for turbulent mixing at the slope. The numerical model (Merrifield and Holloway 2002) indicates a M_2 baroclinic energy flux of $\sim 10GW$ radiating away from the entire Hawaiian Ridge. Klymak et al. (2004), using direct dissipation measurements from 4 different instruments, estimate 7+/-3 GW of turbulent dissipation along the entire Hawaiian ridge. The tidally-generated component of this net dissipation remains to be determined.

To complement the sparse temporal resolution of HOME microstructure measurements near the bottom, deep moorings were deployed near the ridge top and over the flanks of Kaena Ridge, between the islands of Oahu and Kauai. These mooring were designed to sample temperature and current over the first hundreds of meters above the bottom. Indirect estimates of dissipation can be obtained through detection and analysis of turbulent overturns. Levine and Boyd (2005) deployed such a mooring near the ridge top ($1450m$) on the northern flank and found significant overturns linked to tidal phase and amplitude. Levine and Boyd (2005) describe a scenario where the internal tide first strains the mean density field, leading to regions of low N that subsequently overturn. The phase of the tide when overturns occur varies with depth. They found an average dissipation levels of $\sim 10^{-8}Wkg^{-1}$ for the entire experiment. Similar levels of dissipation near the bottom have been reported in direct microstructure measurements (Klymak et al. 2004).

In this paper we examine temperature and current data from a deep ($2425m$) mooring on the southern flank of Kaena Ridge. We use estimates of dissipation based on a Thorpe scale analysis to

show that mixing associated with the semidiurnal internal tide is vigorous at this depth (dissipation events $\geqslant 10^{-7} W kg^{-1}$). The time series provide an unique view of deep mixing driven by a tidal current. The paper is organized as follows. The mooring location and instrumentation are first described in section 2. The observed flow characteristics are discussed in section 3 along with the convention we used to assign semidiurnal phases to the time series. The method for estimating turbulent overturns and the associated dissipation is described in section 4. In section 5 we identify two types of mixing events, related to different phases of the semidiurnal tide, and investigate their relationship with observed shear and strain. In section 6, we propose a generation mechanism for the most energetic type of mixing, based on the observation that the semidiurnal internal tide propagates obliquely relative to the slope. A discussion and summary follow in section 7.

2. Experiment site and data collection

Mooring DS was deployed on the south flank of Kaena Ridge near the $2425m$ isobath (Figures 1 and 2). At this location, the average buoyancy frequency is $0.001 s^{-1}$ and the typical bottom slope is between 1/4 and 1/5. In comparison, the characteristic slope for a M_2 frequency internal wave is between 1/7 and 1/8. The topographic gradient is oriented at a 35° relative to true north. The deployment lasted 87 days between August 16 and November 11, 2002. Swath bathymetry maps (resolution $150m$) show that the mooring was located in a slight depression between two ridges running down the slope and separated by $\sim 10km$. Bottom roughness on scales shorter than $150m$ was not determined.

Numerical model simulations indicate that semidiurnal frequency internal tides are generated near the 1000 m isobath along this portion of the Kaena Ridge (Merrifield et al. 2005). From here,

a portion of the energy takes the form of a downward propagating tidal beam (figure 2). This feature has been observed in microprofiler and expendable current profiler data by (Nash et al. 2004a) and (Lee et al. 2005). The mooring was positioned in the path of the downgoing beam.

The mooring included an upward-looking RDI 300kHz ADCP, $22m$ above the bottom (mab) with a nominal range of approximately $100m$. The ADCP data are 8 minute averages with a vertical resolution of $4m$. The acoustic return from some depth bins was contaminated by the side lobe reflection off the mooring elements, which biases the current speed towards zero. These bins were not used in the analysis, although the data are included in some figures for reference. Reliable current estimates ($\sim 0.02ms^{-2}$ for an 8 minute averaged sample) were obtained out to a range of only 40 to $60m$, presumably due to a low concentration of acoustic scatterers at this depth.

Seabird Electronics temperature sensors (SBE 39) recorded 3 minute averages. The sensors were located between $25mab$ and $220mab$, with sensor spacing varying between 16 and $24m$. The accuracy and resolution of the sensor are $2.10^{-3\circ}C$ and $10^{-4\circ}C$, respectively. For the detection of density inversions it is important to account for any bias errors in the measurements. Averaged over the 3 months of the experiment, temperatures show slight departures from a linear depth profile (Figure 3a). Because tidal motions cause isotherm displacements of $200m$ peak to peak past the mooring sensors, we assume that the sensors sample water with similar properties, and so the departures from a smooth linear profile are taken to be instrument bias errors. We therefore calculate corrections for each of the sensors so that the 3 months averaged vertical profile is linear. We checked for differential sensor drift over time by repeating the corrections based on monthly averages. The results are similar to the 3 month time average, suggesting that differential drift errors are not an important factor. The impact of these corrections on overturn detection is

discussed in section 4).

The sensors at $107mab$ provide a colocated measure of temperature and salinity. We find that temperature and salinity are described adequately by a linear relation at this depth (Figure 3b). Given the range of vertical displacements observed at the sensors, we assume that this relation applies over the $200m$ depth range of the mooring. The salinity at the location of the other sensors is therefore estimated from the linear T-S relation and the potential temperature (calculated for a reference pressure equal to that of the temperature-conductivity sensor). Finally, potential density is calculated for all the sensors, using the same reference pressure. Potential density is used for overturn detection.

3. Current and temperature variability

Time series of current and temperature sampled near the bottom are dominated by fluctuations at semidiurnal frequency (Figure 4). Temperature changes $\geq 0.3°C$ occur during spring tides, and ≤ 0.1°C during neap tides. The horizontal current is stronger in the across-slope direction than the alongslope, with peak speeds of $0.2ms^{-1}$ during springs and $< 0.1ms^{-1}$ during neaps. The alongslope flow is typically $< 0.1ms^{-1}$, although the ratio of across-slope to alongslope varies over the course of the experiment, due to changes in the baroclinic tidal component.

Spectra of horizontal velocity, shear, and buoyancy frequency all show peak energy at the semidiurnal frequency band (Figure 5). Spectral peaks at the diurnal and inertial frequency bands are noticeably smaller than the semidiurnal peak. The semidiurnal band accounts for 60% of the total current variance at each depth, with the M_2 constituent alone accounting for 50% of the variance. Similar ratios are found for vertical shear and temperature. A standard tidal analysis

(Foreman 1978) confirms that the semidiurnal constituents are approximately an order of magnitude larger than the diurnal (Table 1). In general, the M_2 and weaker S_2 constituents create a fortnightly spring-neap cycle (up to a factor of 4 difference in current amplitude).

The current ellipses for the dominant M_2 tidal constituent are directed across the local isobaths (across-ridge). The angle between the topographic gradient and the semimajor axis of the M_2 current ellipses varies between 15° and 30° over the depth range examined (Figure 6). The semimajor axis of the M_2 current is $\sim 0.07 ms^{-1}$ with similar ellipse structure between 45 and 65 mab (Figure 6). Although the current amplitude of the other depth bins is suspect, we include them in figure 6 to show that the orientation and eccentricity of the current ellipses are similar over the depth range. The ellipses also tilt in the across-ridge/depth plane such that the across-ridge flow is parallel to the slope (not shown). Greenwich phases for the current ellipses range from 40° to 50°.

The M_2 barotropic current, predicted either by the POM simulations (Merrifield et al. 2005) or the TPXO model (Egbert 1997) is out of phase with the measured semidiurnal current (Figure 6) . When the semidiurnal surface elevation is high over the ridge, barotropic currents are directed southwestward (Merrifield and Holloway 2002). At this phase of the tide, baroclinic currents along the south flank nearly oppose the barotropic current in model simulations (Merrifield et al. 2005) in agreement with the observed current (Figure 6). This is due to the dominance of the baroclinic tidal current over the barotropic tidal current at these depths. This leads us to conclude that the dominant energy source for tidal motions at the mooring location is the baroclinic component of the tide. A more thorough model-data comparison of near-bottom currents at the DS site will be considered in a later study using a higher resolution model grid (currently $1 - 4km$).

The observed temperature variations (Figure 4) are due primarily to vertical advection of the

background stratification by the semidiurnal tide, with maximum temperatures associated with maximum downward displacements. M_2 temperature variations are converted to vertical displacements using the mean stratification profile obtained from a nearby CTD station. The resulting displacement amplitudes exceed $100m$ at all depths, corresponding to $200m$ peak to peak changes in isotherm depths over a $12.42h$ cycle. Because of the proximity of the bottom boundary, these displacements include a lateral component up and down the slope. Vertical displacement phases show a small increase with distance from the bottom, indicating that displacements near the bottom lead displacements $200m$ above the bottom by approximately 14° (30 minutes). Vertical displacements lag currents by 110°, close to the 90° difference expected for a freely propagating internal tide, and also consistent with the advection of stratified water up and down the slope.

The raw temperature time series are 3 minute averages that are not aligned in time. We interpolate the data to a common 3 minute sample interval and compute potential density. The dataset is then treated as a series of vertical potential density profiles. Each potential density profile is interpolated by a spline function with $1m$ resolution in the vertical, and unstable regions are detected with a tracking algorithm.

Table 1

4. Turbulent overturns, Thorpe scales, and dissipation estimates

The mooring provides a time series of vertical temperature profiles. A noticeable feature of these profiles is the frequent occurrence of statically unstable patches, or turbulent overturns. Figures 7 and 8 show two examples of these overturns. In both cases, the temperature becomes nearly homogeneous over the $200m$ depth range, followed by temperature inversions that affect the entire range. It is therefore impossible to assign a depth to these overturns, other that the middle

of the sampled range. A temperature profile during the overturn shown in figure 8 illustrates the classic s-shaped inversion (figure 9). The inversion far exceeds the rated accuracy of the sensors. In figure 7, the water column slowly restratifies over the remainder of the tidal cycle. In figure 8, the overturning is followed by an abrupt drop in temperature near the boundary, suggestive of a thermal front or tidal bore, followed by a rapid restratification. We will show in section 5) that overturns tend to occur at the two tidal phases depicted in Figures 7 and 8.

The detection and analysis of these turbulent overturns provides an estimate of mixing. Within each detected overturn of vertical size H, the unstable profiles are reordered into stable ones. Each sample ρ_n initially at a depth z_n is assigned a new depth z_m in the reordered profile. The difference $d'_n = z_m - z_n$ is called the Thorpe displacement (Thorpe 1977), and the Thorpe scale is defined as the root mean square of this quantity for each re-ordered overturn :

$$L_T = \overline{(d'^2)}^{1/2} \tag{1}$$

The Thorpe scale can be related to another measure of turbulent dissipation, the Ozmidov length scale (Ozmidov 1965) :

$$L_0 = \epsilon^{1/2} N^{-3/2} \tag{2}$$

Several studies have shown a linear relationship between L_T and L_0 (Dillon 1982; Ferron et al. 1998). Dissipation can be estimated by

$$\epsilon = a^2 N^3 L_T^2 \tag{3}$$

where $a = L_0/L_T$. The value of a used in previous studies varies between 0.65 and 0.95 (see Finnigan et al. (2002) for a review). For the sake of consistency with the mooring study of Levine and Boyd (2005) $a = 0.8$ in this analysis. Levine and Boyd (2005) also discuss the validity of

the Thorpe scale method for estimating dissipation. In Equations 2 and 3, N is obtained from the reordered profile, and therefore is always real.

The smallest detectable overturn is determined by either the vertical spacing between adjacent sensors or the resolution of the sensors (see Finnigan et al. (2002) for more details). At the depth range of interest, we estimate an average of $5.4 \times 10^{-4\circ} C m^{-1}$ for $\frac{\partial T}{\partial z}$. The nominal accuracy of the instruments is $2.10^{-3\circ} C$ (Manufacturer User's manual), so the detection limit based on the sensor accuracy is $3.6m$, much smaller than the sensors spacing. The detection limit is therefore determined by the sensor spacing, which has an upper bound of $24m$. We identify overturns when their height exceeds this value. At the upper limit, overturns exceeding the spacing between the top and bottom sensors ($200m$) are underestimated. Because a sizeable number of the overturn events are characterized by inversions over the entire sample depth (i.e., Figure 10 and 9) , we consider our dissipation estimate to be a lower bound.

Of the 41761 profiles analyzed, 14700 or 34 % contained at least one overturn $> 24m$. The correction applied to the temperature profile (see section 2) minimizes the detection of spurious overturns, arising from sensor errors. For comparison, without the temperature correction, 23000 profiles (or 54 % of the total) contain at least one overturn $> 24m$, but most of these overturns are associated with small temperature differences approaching the accuracy of the sensors (figure 10a). The temperature correction also increases the mean size of small overturns and decreases the size of large overturns (figure 10b). The correction reduces the overall mean dissipation from 3.6×10^{-8} to $1.2 \times 10^{-8} W kg^{-1}$, while the large overturns are responsible for a relatively larger percentage of the dissipation (figure 10c).

Estimated Thorpe scales tend to be large/small during spring/neap tides (figure 11a). Thorpe scales range from 20 to $100m$ for overturns of 24 to $190m$. For each detected overturn of size

H_i, we calculate the dissipation ϵ_i using equation (3). For each profile, the average dissipation for the bottom layer is $\epsilon = \frac{1}{H}\sum \epsilon_i H_i$ where $H = 200m$. Dissipation values range from 10^{-7} to $10^{-6} W kg^{-1}$ during spring tides, and from 10^{-8} to $10^{-7} W kg^{-1}$ during neap tides (figure 11b). The minimum attainable dissipation with this method is $1.2 \times 10^{-10} W kg^{-1}$. The time-averaged dissipation for this $200m$ thick layer is $1.2 \times 10^{-8} W kg^{-1}$. For comparison, Levine and Boyd (2005) found average dissipations of $10^{-8} W kg^{-1}$ for a 300m thick layer above the 1450m isobath. Our average dissipation value should be treated with caution. Changes in the analysis method can lead to sizeable changes in the average. For example, a spline instead of a linear interpolation of the measurements leads to a 25% increase in the mean dissipation value. As already noted, the bias correction reduces the dissipation by 67%. We have attempted to make analysis choices that minimize the average dissipation.

Following Osborn (1980), we compute the vertical eddy diffusivity coefficient K_ρ by assuming that the turbulent kinetic energy balance is between shear production, buoyancy loss and turbulent dissipation :

$$K_\rho = \Gamma \epsilon N^{-2} \tag{4}$$

The mixing efficiency Γ is taken equal to 0.2, and N is now the background stratification. Converting the estimated dissipation values in this way, we obtain a time-averaged eddy diffusivity of $2 \times 10^{-3} m^2 s^{-1}$, two orders of magnitude higher than typical open ocean estimates at this depth. For comparison, Klymak et al. (2004) found values of up to $10^{-2} m^2 s^{-1}$ near the ridge top, and Levine and Boyd (2005) found values of $10^{-3} m^2 s^{-1}$ near the bottom at their mooring site.

5. Dissipation Events and the Semidiurnal Tide

Because the observations are dominated by oscillations at the M_2 frequency, we divide the time series into 163 M_2 cycles to investigate the mixing events in relation to tidal phase. A complex demodulation of the horizontal velocity is used to transform time into M_2 phase. With this convention, upslope flow occurs for phases between -90° and 90°, downslope flow occurs during the rest of the cycle. We then ensemble-average with respect to phase to obtain composites of temperature, velocity and dissipation over the M_2 tidal cycle (figure 12).

Enhanced dissipation occurs during two distinct phases of the tidal cycle (shaded areas on figure 12). The first is centered around 140° and is associated with maximum downslope flows, increasing water temperatures, and low stratification. We refer to this mixing phase as "downslope flow mixing". Figure 7 is an example of a downslope flow mixing event. The second peak, centered around -90°, is associated with the flow reversal from upslope to downslope, maximum water temperatures, and increasing stratification with a pronounced local minimum. We refer to this phase as "flow reversal mixing". Figure 8 is an example of a flow reversal mixing event.

Although observed mixing events are linked to tidal phase, they do not occur as regularly as the tide itself. To illustrate the variability of tidal mixing, we visually inspect each M_2 cycle and assign the cycle to one of five categories: "downslope flow mixing only" when dissipation occurs near the maximum downslope current, "flow reversal only" when dissipation occurs at the reversal from down to upslope flow, "both downslope flow mixing and flow reversal" when both events occur during the same cycle, "no mixing" when dissipation failed to reach a threshold value of $0.5 \times 10^{-7} W kg^{-1}$, and "random mixing event" when dissipation events occur at other phases of the tide. We find that 63% of the tidal cycles contain flow reversal and/or downslope flow mixing, 21 % of the time series have no significant mixing, and 16 % show only odd mixing events. Tidal cycles containing flow reversal mixing events account for 40% of the total estimated dissipation,

downslope flow events account for 20%, combined events 21%, and random events 16%. Although downslope flow mixing events appear throughout the experiment, flow reversal mixing events are nearly absent during the first spring-neap cycle, and their occurence and amplitude appear to increase over time (figure 13a). We attribute this increase in part to the increase in semidiurnal current amplitude (figure 11). In addition, the first spring-neap cycle is characterized by more circularly polarized tidal currents than the other cycles (figure 13b). We will return to this point when considering the cause of flow reversal mixing events in section 6.

We next consider whether tidal shear and strain act to trigger mixing events, in the manner of a shear instability. We calculate the shear over the depth range 41 to $65mab$. Again, the ADCP only samples a small fraction of the 200 m length of the thermistor chain. *We also note that the shear over this depth range can represent a combination of boundary flow induced shear, and turbulent shear from the overturns. The poor resolution of the current measurement does not allow for further separation between boundary shear and turbulent shear*. N is computed averaged over the same range as the ADCP, and also over the full range of the thermistors (27 to $220mab$).

Representative downslope flow mixing events (figure 14) occur during each semidiurnal cycle near the time of maximum downslope flow. Flow reversal mixing events are absent during the time period. Downslope flow mixing occurs when the stratification is at a minimum, or equivalently the strain is a maximum, over the tidal cycle. Tidal current shear tends to peak twice during the cycle at both up and downslope flow (figure 14 b and c); however, the combination of high shear and strain during the downslope phase results in an inverse Richardson number highly correlated with the dissipation events (figure 14 b and d). The results are similar using different depth ranges for computing N (i.e. $20m$ versus $200m$). Figure 14c) shows the results using N averaged over 200m because it is less noisy than that based on a 20m average. We conclude that downslope flow

mixing events are the result of shear instability.

At other time periods, flow reversal mixing events are dominant and noticeable downslope flow events are absent (figure 15). Strong flow reversal mixing events occur every other semidiurnal cycle. There are also other periods (not shown) when moderate flow reversal events occur at every semidiurnal cycle. In sharp contrast to downslope flow mixing, flow reversal mixing events do not coincide with elevated shear or elevated inverse Richardson number (figure 15 c and d). Similar results are obtained using N averaged over the common 20m depth range as shear, and also using shear and strain computed over 10m spacings. Stratification minima occur during the events at a phase of the tidal cycle when the stratification would otherwise be increasing (figure 15 b) . The stratification begins to decrease approximately one hour before the main overturning event. This increased strain occurs because of a phase lag of the temperature signal with depth. Inspection of the temperature record for a typical event (figure 15 a) shows that the isotherms begin to converge prior to mixing because temperatures decrease in the upper water column (150 to 220 mab) one hour before the lower water column (27 to 75 mab). In the lower water column, the measured currents and temperature are consistent in that temperatures increase during downslope flows. In the upper water column, we do not have reliable current measurements to confirm that the early temperature decrease is due to a change to upslope currents.

The poor relationship between flow reversal mixing events and shear or Richardson number may be due to the lack of reliable observations above 65 mab. For example, a shear instability occurring above 65mab may create an overturn that is advected into the sample range. We believe this is unlikely, however, because the event is characterized by a strong temperature decrease suggestive of a tidal bore. Mixing of warmer waters above the mooring would not result in the generation of waters dense enough to impact the mooring in the sense of a gravity current. Further-

more, the background currents are near zero or directed upslope (i.e., at flow reversal or shortly thereafter). The character of the temperature signal strongly suggests that cold water downslope of the mooring has been uplifted above the mooring, resulting in the instability. Levine and Boyd (2005) also observed mixing associated with the semidiurnal tide to occur at two distinct phases on the north side of Kaena Ridge at $1500m$ depth. In their case, overturns near $100mab$ occur at 180 degrees out of phase with overturns near $300mab$, both related to enhanced strain. Our observations differ in that we see overturns at two tidal phases, but in the same depth range.

For both mixing types, strain appears to be an important precursor to overturning. For downslope flow mixing, overturns occur during the maximum strain over the semidiurnal tidal cycle (figure 12 and 14). For flow reversal mixing, overturns occur during a secondary strain maximum that is out of phase with the semidiurnal cycle. Over the entire dataset, the correlation between the strain and dissipation is insignificant (0.19); however, when calculated for a subrecord when downslope flow mixing is dominant (the 3 days shown on figure 14), this correlation improves (0.45). For subrecords of similar length, at times when flow reversal mixing is dominant, the correlation between the strain and dissipation does not exceed 0.2 . Tidal current shear, at least over the measured depth range, is not significantly correlated with dissipation, even over short periods when only one mixing type is observed (figure 14 and 15). Combining the effects of shear and strain, in the form of an inverse Richardson number, does not improve the correlations obtained using strain alone, which again highlights the primary importance of strain for downslope flow events, and further discounts shear instability as a mechanism for flow reversal events.

6. Obliquely propagating internal tides and mixing

Gemmrich and van Haren (2001) documented the occurence of thermal fronts near the bottom boundary in $\sim 850m$ depth along the Bay of Biscay continental slope. They describe abrupt temperature change, linked to the presence of an internal tide beam propagating downward at an oblique angle relative to the slope. Gemmrich and van Haren (2001) hypothesized that the obliquely propagating internal tide results in a variation of tidal phase along isobaths, particularly if the internal tide is in the form of a narrow beam. The variable phase of the tidal currents can advect cold water upslope above warm water once per tidal cycle, creating sharp thermal fronts and convective instability. The oblique propagation angle is crucial; an internal tide propagating directly downslope would not generate such unstable fronts. Gemmrich and van Haren (2001) observed sharp temperature drops associated with the collapse and/or passage of these fronts. In contrast to the studies of the reflection of internal tides normally incident on a sloping boundary (Nash et al. 2004b; Legg and Adcroft 2003), the mechanism identified by Gemmrich and van Haren (2001) relies on downgoing internal tides that propagate obliquely along the slope.

Similarities between the Bay of Biscay and the Kaena Ridge observations suggest that this mechanism may explain the mixing events documented here as "flow reversal mixing". First, for both experiment sites, the observations were made over a supercritical slope for the semidiurnal tide, which allows a tidal beam genererated at a ridge crest or shelf break to propagate downward without reflection. Such a beam would propagate farther from the slope with increasing depth; however, Gemmrich and van Haren (2001) describe how obliquely propagating waves still can intersect the slope. This is apparently also the case at the Kaena Ridge : The observed tidal currents are oriented at an angle relative to the slope (figure 12), consistent with a tidal beam with an oblique propagation azimuth. Following Gemmrich and van Haren (2001), this could lead to the generation of fronts with an angle φ between 54° and 80° relative to the isobaths ($N = 1e^{-6}s^{-2}$,

the topographic slope $\alpha = 18.6°$, the M_2 vertical propagation angle is $7.5°$, and the angle between the isobath and the bottom projection of the group velocity vector is between $40°$ and $80°$). During the first spring-neap cycle, when flow reversal mixing events are not detected, the current ellipse is more circularly polarized than during the subsequent cycles (figure 13b). It appears that a circular current ellipse, as opposed to a more unidirectional flow, is not conducive to this overturning mechanism.

Second, the temperature data from the Bay of Biscay and the Kaena Ridge bear a striking resemblance (our figure 8 and figure 4 in Gemmrich and van Haren (2001)). The temperature drops sharply at the time of flow reversal from down to upslope, which Gemmrich and van Haren (2001) characterized as a passing thermal front. The similarities are particularly striking near the bottom, (Gemmrich and van Haren (2001) observations were all below $50mab$). Higher in the water column ($\geq 100mab$), above the elevations sampled in the Bay of Biscay, we see evidence for strong restratification following the front passage.

Third, tidally driven convection is an attractive mechanism for flow reversal events given that tidal current and current shears are weak during this phase of the tide. Enhanced strain, which is observed preceding mixing events (figure 8), can also be a signature of a developing convective instability rather than a shear instability.

Lastly, the dependence of this mechanism on the location of the internal tide beam relative to the mooring (figure 6 in Gemmrich and van Haren (2001)) can also explain the intermittent nature of the observed mixing events. At our Kaena Ridge site, low dissipation is associated with low tidal amplitude, but high tidal amplitude is not always associated with strong dissipation (figure 11). Our analysis has focused on the relationship of mixing events to the measured tidal currents. We emphasize that the measured tide is dominated by the baroclinic component at the mooring

location, (figure 12 c). The observed increase in amplitude of the semidiurnal currents (figure 11c), and the change in eccentricity over the duration of the experiment (figure 13b) presumably are attributed to changes in the internal tide. Low frequency currents and changes in stratification higher in the water column, between the mooring location and the generation site near the ridge top, can cause temporal changes in amplitude, phase, position or direction of the internal tide, which apparently influence the level of convective mixing observed at the fixed moored location (figure 13a).

7. Summary and Discussion

In this field experiment, we find that the semidiurnal tide dominates the current and temperature variability above the steep flanks of the Kaena Ridge. In particular, near-inertial wave energy, diurnal tides, and subinertial currents, which might contribute to near boundary mixing due to bottom drag, are all much weaker than the semidiurnal tide. The predominance of the semidiurnal tide and lack of diurnal tide energy are consistent with their respective predicted ray paths from the model simulations of Merrifield et al. (2005). Barotropic to baroclinic tidal conversion near the top of Kaena Ridge results in downward propagating tidal beams that are the primary source of mechanical energy for the ridge.

Overturns and the implied associated mixing and dissipation occur predominantly at two phases of the measured semidiurnal tidal cycle: when flows are near maximum in the downslope direction, and at the flow reversal prior to upslope flow, at maximum downward isopycnal displacements. The mechanism causing the downslope flow mixing events appears to be a shear instability, triggered primarily by high strain, occurring when stratification is minimum over the

tidal cycle. Levine and Boyd (2005) find a similar relationship between mixing events and strain at a shallower depth on the ridge. Flow reversal mixing occurs during high strain conditions that do not coincide with the tidal strain maximum. These events appear unrelated to shear, and the associated dissipation is poorly correlated with the inverse Richardson number, suggesting that shear instability is not the primary generation mechanism. Based on similarities with observations made by Gemmrich and van Haren (2001) in the Bay of Biscay, we suspect that the flow reversal mixing events are convectively driven. In this scenario, mixing develops because of the oblique propagation angle of the downward propagating internal tide relative to the slope. This leads to the advection of cold water above warm water along the slope, the generation of a sharp thermal front, and eventually to statically unstable conditions and overturning. Evidence supporting this hypothesis includes the observed orientation of the internal tide relative to the slope, the abrupt temperature decrease associated with the overturn, and the poor correspondence with tidal shear. The enhanced strain preceding these events may result from the development of a statically unstable patch.

Ultimately, we seek a tidal mixing parameterization that can be incorporated into regional numerical models, so that estimates of deep mixing can be extrapolated to the entire ridge system, as well as to other locations. We might expect that the mixing associated with the tide would have a high predictability. Although the internal tide provides most of the mechanical energy at this site, a few tidal consituents explain a significant fraction of the observed variability, presumably due to the proximity of the mooring to the generation site(s). Although both mixing events are linked to the tide, neither is as predictable as the tide itself. Downslope flow mixing events exhibit a visual correspondence with inverse Richardson number, however, at best the correlation is only 0.4. This may be due to limitations in our current measurements, which only resolved shear over a

small fraction of the overturning depth range. We believe that a traditional mixing parametrization based on tidal strain and shear may be useful to explain downslope flow mixing.

If flow reversal mixing is caused by convective instabilities in the manner described by Gemmrich and van Haren (2001), a mixing parametrization is more complicated. Predictability would depend on the orientation of the internal tide relative to the topography, which in turn requires detailed knowledge of how changes in the background stratification and currents affect the generation and propagation of the internal tide. Small changes in the propagation azimuth of the internal tide presumably would lead to significant changes in mixing.

In the context of the other HOME observations at Kaena Ridge, we find good agreement between our inferred dissipation rates based on Thorpe scales and direct microstructure measurements. Our estimated time-averaged dissipation is $1.2 \times 10^{-8} W kg^{-1}$, but can reach up to $10^{-6} W kg^{-1}$. The corresponding time-averaged eddy diffusity is $2 \times 10^{-3} m^2 s^{-1}$. For comparison, Levine and Boyd (2005) and Klymak et al. (2004) found comparable average dissipation values of $2 \times 10^{-8} W kg^{-1}$ at the $1450m$ isobath and $4 \times 10^{-9} W kg^{-1}$ at $3000m$ respectively. The microstructure measurements suggest that mixing rates are enhanced 100 to $200 mab$ near the bottom (Klymak et al. 2004). Given the sporadic and event-like nature of the mixing, the value of continuous sampling over time for estimating mixing is highlighted by our observations. It is remarkable that the two methods of estimating mixing, microstructure profiles versus overturns from continuous temperature time series, give such consistent results.

Rainville and Pinkel (2005), using data obtained on the ridge crest from FLIP (figure 1), found enhanced strain at diurnal, not semidiurnal timescales. They conclude that Parametric Subharmonic Instabilities (PSI) are an important pathway from the semidiurnal tide to small scales. Here we find enhanced shear and strain only at semidiurnal frequencies. This suggests that PSI may

be an important mechanism over the ridge (Rainville and Pinkel 2005; Carter and Gregg 2005), but apparently not over the deep ridge flanks. We note that our study site is below the main thermocline, within a depth range that has been a focus of abyssal mixing studies (Munk and Wunsch 1998). The preliminary HOME results from Kaena Ridge encourage speculations that tidally-driven mixing mechanisms may differ above and below the main thermocline.

Finally, these results are not necessarily specific to Hawaii, or even ridge topographies. Internal tides are generated at many continental shelf breaks, and combined with supercritical or critical continental slopes, downgoing tidal beams are likely to interact with the topography. The relative importance of tidally-driven shear instability and convective mixing, as described by Gemmrich and van Haren (2001), remains to be determined. Given the large fraction of continental slope worldwide where downgoing tidal beams are potentially present, we speculate that these beams may account for a significant fraction of the mixing occuring at deep oceanic boundaries. This mechanism has received less attention than the critical reflections of incident internal tides.

Future work will include an analysis of mooring data from a later deployment on the north flank of the ridge, as well as 12 hour repeat surveys of the bottom boundary layer made using CTD and a lowered ADCP. Based on these analyses and comparisons with numerical simulations of the internal tide, we hope to gain a better understanding of flow reversal mixing along the deep flanks of the Hawaiian Ridge.

Acknowlegments

The successful deployment and recovery of our HOME moorings from the R/V Wecoma under sometimes adverse conditions was achieved in large part due to the skill and knowledge of

Captain Dan Arnsdorf, Asst. Engineer Duane Leafdahl, Marine Technician Daryl Swensen, and the entire crew. We also thank Walt Waldorf for his expert assistance in deploying and recovering the moorings. Eric Firing provided helpful advice in analyzing the ADCP data. Discussions with Murray Levine, Tim Boyd, and the other HOME investigators are greatly appreciated. The suggestions from two anonymous reviewers significantly improved the presentation and interpretation of the results. We appreciate the support of the National Science Foundation through grant OCE-9819533 and OCE9819519, and the efforts of program manager Eric Itsweire in facilitating the HOME project.

REFERENCES

Armi, L., 1978: Some evidence for boundary mixing in the deep ocean. *J. Geophys. Res.*, **83**, 1971–1979.

— 1979: Reply to comments by C. Garrett. *J. Geophys. Res.*, **84**, 5097–5098.

Carter, G. S. and M. C. Gregg, 2005: Persistent near-diurnal internal waves observed above a site of m2 barotropic-to-baroclinic conversion. *J. Phys. Oceanogr.*.

Dillon, T. M., 1982: Vertical overturns : A comparison of Thorpe and Ozmidov length scales. *J. Geophys. Res.*, **87**, 9601–9613.

Dushaw, B. D., B. M. Howe, B. D. Cornuelle, P. F. Worcester, and D. S. Luther, 1995: Barotropic and baroclinic tides in the central north pacific ocean determined from long-range reciprocal acoustic transmissions. *J. Phys. Oceanogr.*, **25**, 631–647.

Egbert, G., 1997: Tidal data inversion : Interpolation and inference. *Prog. Oceanogr.*, **40**, 53–80.

Egbert, G. and R. D. Ray, 2000: Significant dissipation of tidal energy in the deep ocean infered from satellite altimeter data. *Nature*, **405**, 775–778.

Eriksen, C., 1998: Internal wave reflection and mixing at Fieberling Guyot. *J. Geophys. Res.*, **103**, 2977–2994.

Ferron, B., H. Mercier, K. Speer, A. Gargett, and K. Polzin, 1998: Mixing in the Romanche fracture zone. *J. Phys. Oceanogr.*, **28**, 1929–1945.

Finnigan, T., D. Luther, and R. Lukas, 2002: Observations of enhanced diapycnal mixing near the Hawaiian ridge. *J. Phys. Oceanogr.*, **32**, 2988–3002.

Foreman, M. G. G., 1978: Manual for tidal currents analysis and prediction. Technical report, Pacific Marine Science Report.

Garrett, C., 1991: Marginal mixing theories. *Atmosphere-Ocean*, **29**, 313–339.

Gemmrich, J. R. and H. van Haren, 2001: Thermal fronts generated by internal waves propagating obliquely along the continental slope. *J. Phys. Oceanogr.*, **31**, 649–655.

Gregg, M. C., 1991: The study of mixing in the ocean: A brief history. *Oceanography*, **4**, 39–45.

Gross, T. F., A. J. Williams III, and W. D. Grant, 1986: Long-term in situ calculations of kinetic energy and Reynolds stress in a deep sea boundary layer. *J. Geophys. Res.*, **91**, 8461–8469.

Hasumi, H. and N. Suginohara, 1999: Effects of locally enhanced vertical diffusivity over rough bathymetry on the world ocean circulation. *J. Geophys. Res.*, **104**, 23,637 – 23,374.

Klymak, J. M., J. N. Moum, J. D. Nash, E. Kunze, J. B. Girton, G. S. Carter, C. M. Lee, T. B. Sanford, and M. C. Gregg, 2004: An estimate of tidal energy lost to turbulence at the hawaiian ridge. *Submitted to J. of Phys. Oceanogr.*.

Kunze, E. and J. M. Toole, 1997: Tidally driven vorticity, diurnal shear, and turbulence atop fieberling seamount. *J. Phys. Oceanogr.*, **27**, 2663–2693.

Lee, C. M., E. Kunze, T. Sanford, J. D. Nash, M. A. Merrifield, and P. E. Holloway, 2005: Internal tides and turbulence along the 3000-m isobath of the hawaiian ridge with model comparisons. *Submitted to J. of Phys. Oceanogr.*.

Legg, S. and A. Adcroft, 2003: Internal wave breaking at concave and convex continental slopes. *J. Phys. Oceanogr.*, **33**, 2224–2246.

Levine, M. D. and T. J. Boyd, 2005: Tidally-forced internal waves and overturns observed on a slope : Results from the HOME survey component. *Submitted to J. of Phys. Oceanogr.*.

Lien, R.-C. and M. C. Gregg, 2001: Observations of turbulence in a tidal beam and across a coastal ridge. *J. Geophys. Res.*, **106**, 4575–4592.

Lukas, R., F. Santiago-Mandujano, F. Bingham, and A. Mantyla, 2000: Cold bottom water events observed in the Hawaii Ocean Time-series: Implications for vertical mixing. *Deep-Sea Res.*,

48, 995–1021.

Merrifield, M. A. and P. E. Holloway, 2002: Model estimates of M2 internal tide energetics at the Hawaiian ridge. *J. Geophys. Res.*, **107**, 10.1029/2001JC000996.

Merrifield, M. A., K. Katsumata, P. E. Holloway, Y. L. Firing, and N. Zilberman, 2005: Model simulations of baroclinic tides at kaena ridge, hawaii. *Submitted to J. of Phys. Oceanogr.*.

Munk, W. H., 1966: Abyssal recipes. *Deep-Sea Res.*, **13**, 207–230.

Munk, W. H. and C. Wunsch, 1998: Abyssal recipes II : energetics of tidal and wind mixing. *Deep-Sea Res.*, **45**, 1978–2010.

Nash, J. D., E. Kunze, C. M. Lee, and T. B. Sanford, 2004a: Structure of the baroclinic tide generated at kaena ridge, hawaii. *Submitted to J. of Phys. Oceanogr.*.

Nash, J. D., E. Kunze, J. M. Toole, and R. W. Schmitt, 2004b: Internal tide reflection and turbulent mixing on the continental slope. *J. Phys. Oceanogr.*, **34**, 1117–1134.

New, A. L. and R. D. Pingree, 1990: Evidence for internal tidal mixing near the shelf break in the bay of biscay. *Deep-Sea Res.*, **37**, 1783–1804.

Osborn, T. R., 1980: Estimates of the local rate of vertical diffusion from dissipation measurements. *J. Phys. Oceanogr.*, **10**, 83–89.

Phillips, O. M., J. Shyu, and H. Salmun, 1986: An experiment on boundary mixing : mean circulation and transport rates. *J. Fluid Mech.*, **173**, 473–499.

Polzin, K. L., J. M. Toole, J. R. Ledwell, and R. W. Schmitt, 1997: Spatial variability of turbulent mixng in the abyssal ocean. *Science*, **276**, 93–96.

Rahmstorf, S., 2003: The current climate. *Nature*, **421**, 699.

Rainville, L. and R. Pinkel, 2005: Baroclinic energy flux at the hawaiian ridge: Observations from the R/P FLIP. *J. Phys. Oceanogr.*.

Ray, R. D. and G. T. Mitchum, 1996: Surface manifestation of internal tides generated near Hawaii. *Geophys. Res. Letters*, **23**, 2101–2104.

Samelson, R. M., 1998: Large scale circulation with locally enhanced vertical mixing. *J. Phys. Oceanogr.*, **28**, 712–726.

Simmons, H. L., S. Jayne, L. S. Laurent, and A. Weaver, 2004: Tidally driven mixing in a numerical model of the ocean general circulation. *Ocean Modelling*, **6**, 245–263.

Thorpe, S. A., 1977: Turbulence and mixing in a Scottish Loch. *Phil. Trans. R. Soc. Lond.*, **286**, 125–181.

— 1999: 75+25=99, or some of what we still don't know: Wave groups and boundary processes. *Aha Huliko'a Hawaii Winter Workshop*.

Toole, J. M., R. W. Schmitt, K. L. Polzin, and E. Kunze, 1997: Near-boundary mixing above the flanks of a midlatitude seamount. *J. Geophys. Res.*, **102**, 947–959.

Wunsch, C., 2000: Moon, tides and climate. *Nature*, **405**, 743–744.

Figures

FIG. 1

FIG. 2

FIG. 3

FIG. 4

FIG. 5

FIG. 6

FIG. 7

FIG. 8

FIG. 9

FIG. 10

FIG. 11

FIG. 12

FIG. 13

FIG. 14

FIG. 15

Generated with ametsocjmk.cls.
Written by J. M. Klymak
mailto:jklymak@ucsd.edu
http://opg1.ucsd.edu/ jklymak/WorkTools.html

Tables

Tidal constituent	O1	K1	N2	M_2	L2	S2
m/s	0.0055	0.003	0.025	0.074	0.01	0.029
Greenwich Phase	341	286	83	52	324	89
$\times 10^{-3o}C$	7.1	2.2	27	63.5	4.6	14.2
Greenwich Phase	262	133	337	294	234	338

Table 1. Contribution of the main diurnal and semidiurnal tidal constituents for horizontal velocities at 65 mab (top) and temperature at 60 mab (bottom)

Figure Captions

FIG. 1. Bathymetric map of the Kaena Ridge showing the locations of the DS mooring (this study), the Big Boy mooring (Levine and Boyd 2005), and FLIP (Rainville and Pinkel 2005).

FIG. 2. A cross-section of the ridge, in the approximate location of DS, showing estimates of M_2 baroclinic energy flux from Merrifield et al. (2005). The mooring is located in the path of a downgoing tidal beam. The stratification profile (right panel) is from a nearby CTD station occupied during the mooring deployment. The small inset (drawn to scale) shows the mooring location, and the larger inset shows the location on the mooring line of temperature (T) and current (C) measurements.

FIG. 3. a) Temperatures averaged over the entire deployment show small departures from a linear profile, which are interpreted as instrument bias errors. b) : The distribution of temperature and salinity measured at 2317 m depth, 107 meters above the bottom (mab). The black line is a linear fit of the data.

FIG. 4. A representative 14 day time series of temperature ($75mab$), across-slope and along-slope currents ($65mab$).

FIG. 5. Power spectra of a) horizontal current at $65mab$, b) temperature ($220mab$ and $27mab$), c) vertical shear of the horizontal current (between 40 and $65mab$), d) depth-averaged buoyancy frequency (27 to $220mab$). Top abscissa is in cycles per day (cpd).

FIG. 6. The M_2 (left) and S_2 (right) measured horizontal current ellipses, with suspect depth bins in gray (i.e., side lobe contamination problems). Barotropic current ellipses predicted by the TPXO model (Egbert 1997) are depicted at the top. The direction of the topographic gradient is indicated with the gray arrow on the left.

FIG. 7. A characteristic overturn event depicted in 12 hour time series (day 233) of a) potential temperature recorded at 27, 43, 59, 75, 91, 107, 124, 147, 171, 195, and 220 mab, with darker lines correpsonding to smaller elevations above the bottom, b) estimated dissipation (ϵ, equation 3, thin gray line) and depth-averaged buoyancy frequency (27 to $220mab$, thick black line), and c) horizontal currents, rotated so that across-slope velocity is vertical. Depth bins with suspect side lobe contamination are shown in gray.

FIG. 8. Same as figure 7 for day 249, showing an overturn during a different phase of the tide.

FIG. 9. a) Vertical profile at day 249, hour 11.5 (figure 8) of measured absolute temperature after removing of long term bias. '*' indicate the locations of the instruments. Thin lines represent the measurement plus or minus the nominal accuracy of the instruments. b) infered potential density ($-1000kgm^{-3}$).

FIG. 10. a) The distribution of the number of overturns, before and after the temperature correction, as a function of the observed temperature difference across the depths of the overturn. b) The distribution of overturn size as a function of the temperature difference across the overturn. c) The distribution of the percentage of the total dissipation contributed by the overturns, as a function of the temperature difference across the overturn.

FIG. 11. a)The estimated Thorpe scale (L_T), b) dissipation (ϵ), and c) the measured semidiurnal tidal amplitude using horizontal currents at $65mab$.

FIG. 12. A composite semidiurnal tidal cycle, obtained using ensemble phase averages over the entire time series, of a) potential temperature recorded at 27, 43, 59, 75, 91, 107, 124, 147, 171, 195, and 220 mab, with darker lines correpsonding to smaller elevations above the bottom, depth averaged buoyancy frequency (27 to $220mab$, dashed black line), b) estimated dissipation (ϵ, equation 3), and c) horizontal currents, rotated so that across-slope velocity is vertical. Depth bins with suspect side lobe contamination are shown in gray. Estimates of the barotropic current (TPXO (Egbert 1997)) are included. Shaded areas indicate phases of intense mixing associated with downslope flow (dark), and flow reversal (light).

FIG. 13. a) Dissipation (ϵ), averaged over a semidiurnal cycle, is classified in terms of the dominant mixing types that occur during the cycle. b) The eccentricity of the semidiurnal current ellipse, quantified as the ratio of the minor over the major axis current amplitude. Ellipse amplitudes are obtained from a harmonic analysis of 7 days subrecords.

FIG. 14. Downslope flow mixing events in 3 day time series of a) potential temperature, b) depth-averaged buoyancy frequency N (27 to $220mab$, thick black line), and estimated dissipation (thin gray line), c) square of the horizontal current shear (from 41 to $65mab$), d) inverse Richardson number (from shear and N above), and e) the horizontal velocity (at $65mab$).

FIG. 15. Same as figure 14 for a period of flow reversal mixing events. .

Figures

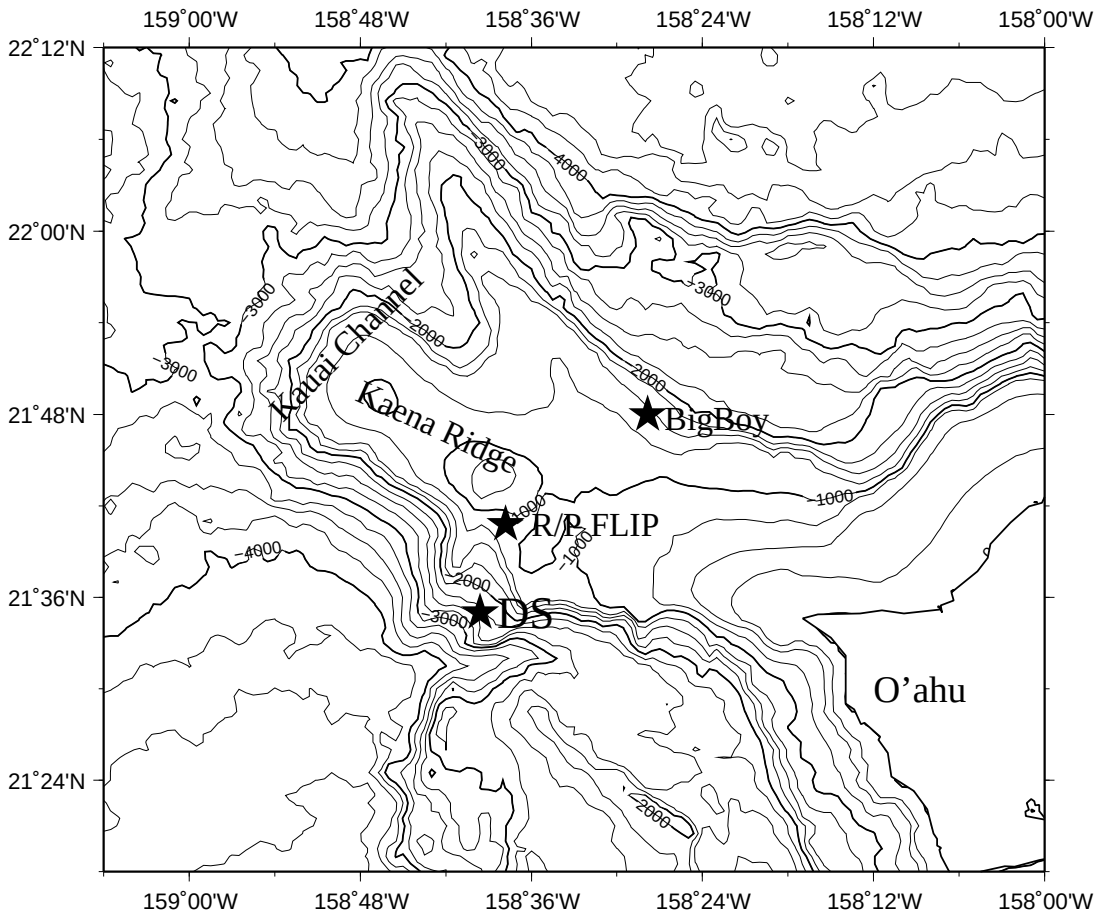

FIG. 1. Bathymetric map of the Kaena Ridge showing the locations of the DS mooring (this study), the Big Boy mooring (Levine and Boyd 2005), and FLIP (Rainville and Pinkel 2005).

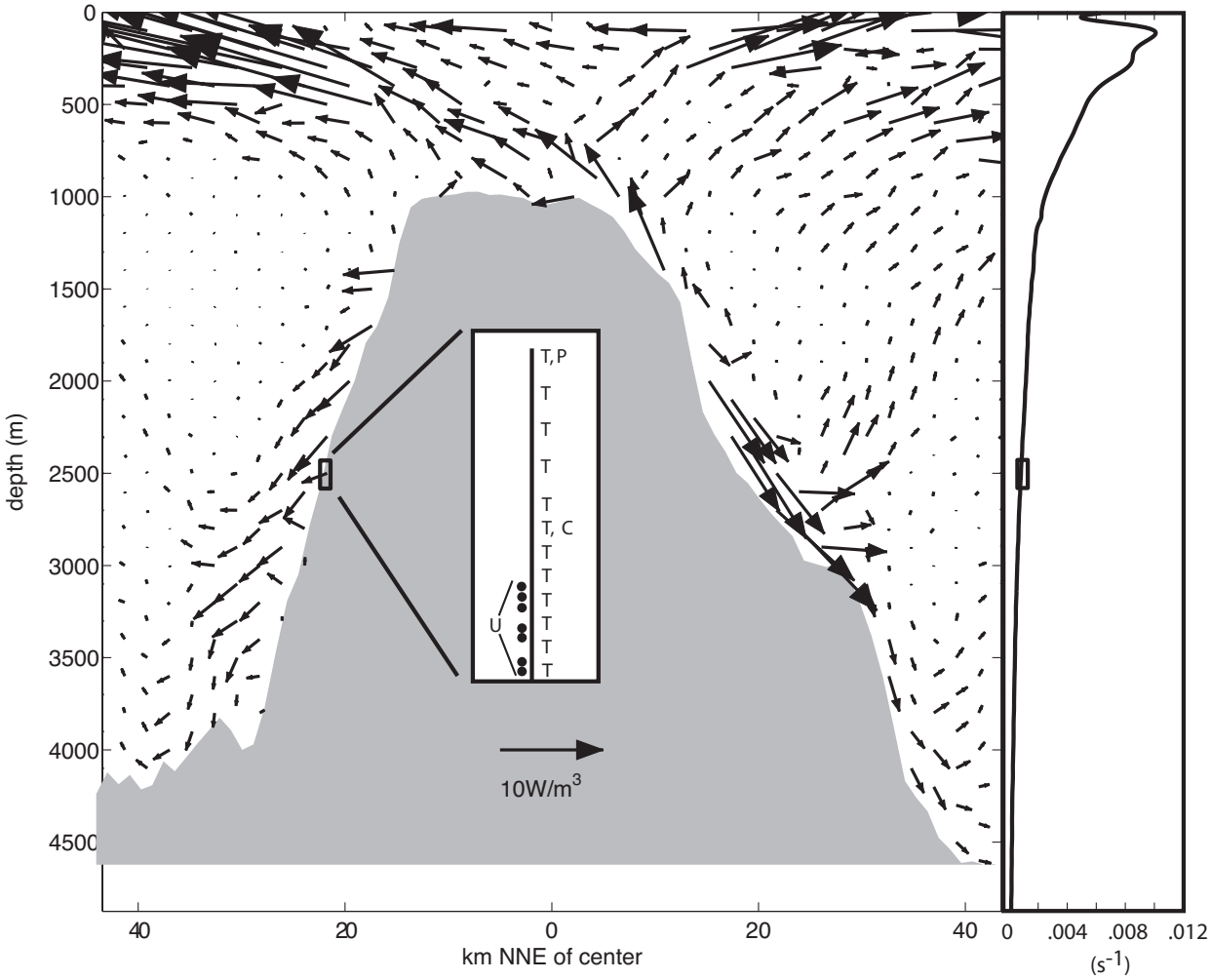

FIG. 2. A cross-section of the ridge, in the approximate location of DS, showing estimates of M_2 baroclinic energy flux from Merrifield et al. (2005). The mooring is located in the path of a downgoing tidal beam. The stratification profile (right panel) is from a nearby CTD station occupied during the mooring deployment. The small inset (drawn to scale) shows the mooring location, and the larger inset shows the location on the mooring line of temperature (T) and current (C) measurements.

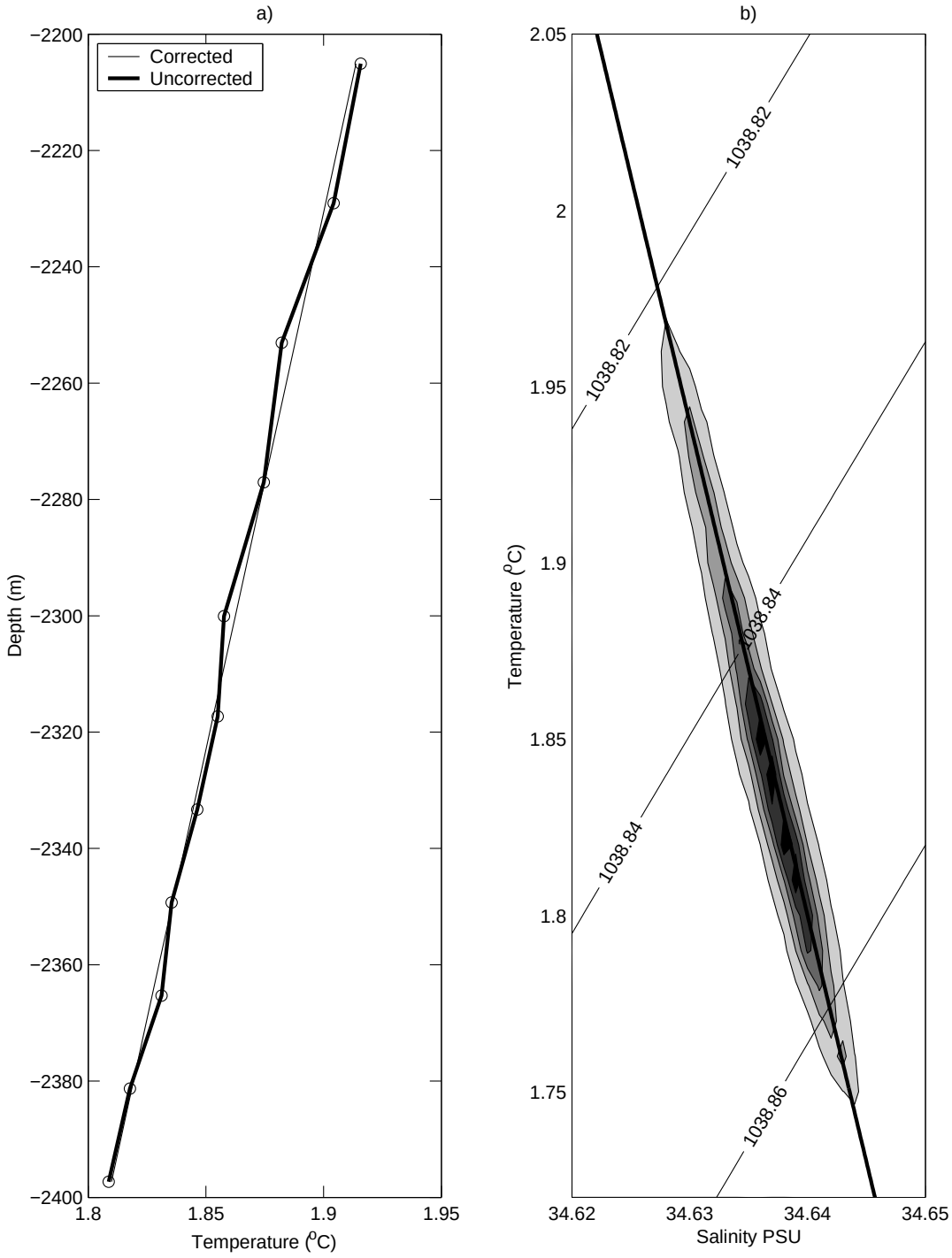

FIG. 3. a) Temperatures averaged over the entire deployment show small departures from a linear profile, which are interpreted as instrument bias errors. b) : The distribution of temperature and salinity measured at 2317 m depth, 107 meters above the bottom (mab). The black line is a linear fit of the data.

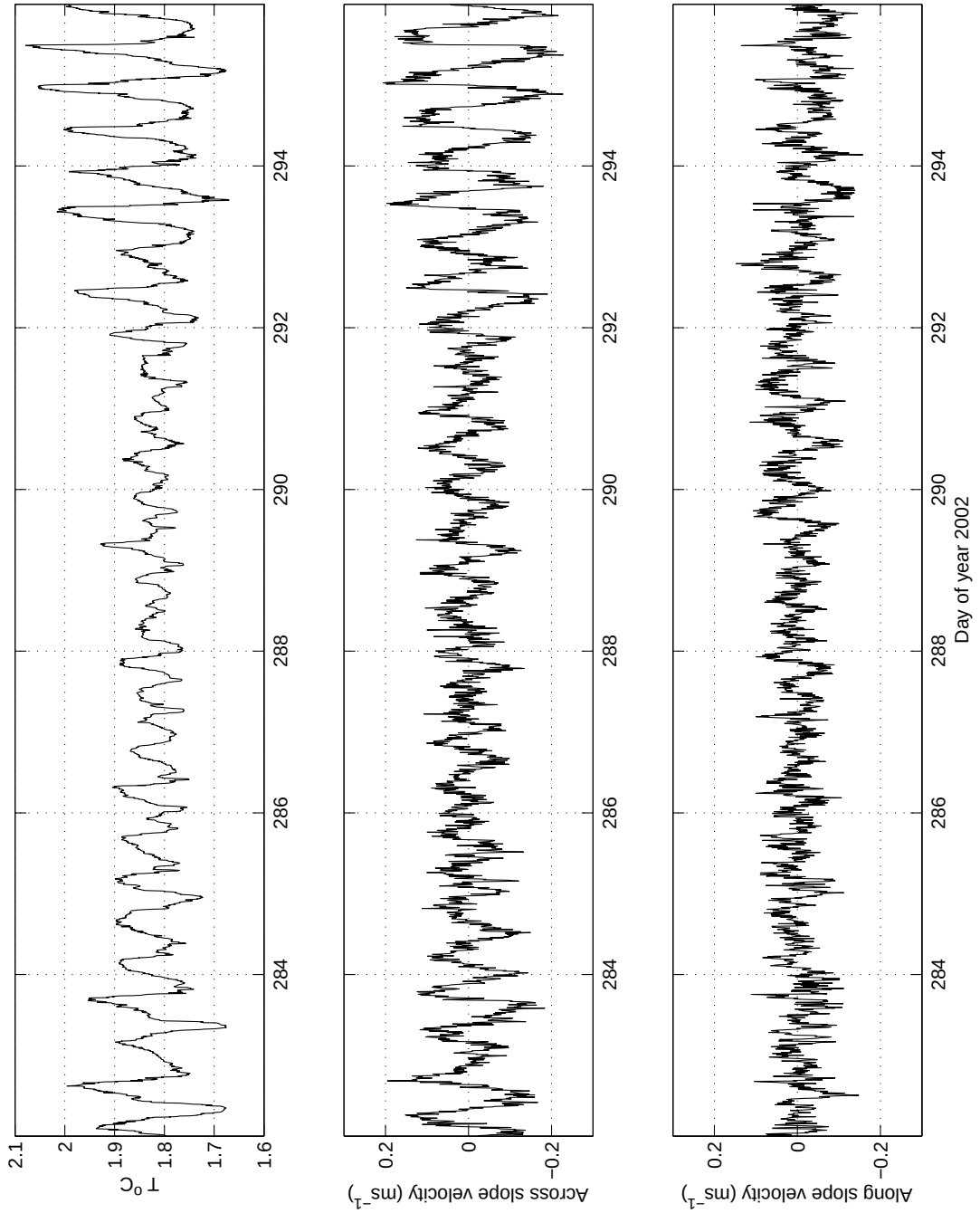

FIG. 4. A representative 14 day time series of temperature ($75mab$), across-slope and along-slope currents ($65mab$).

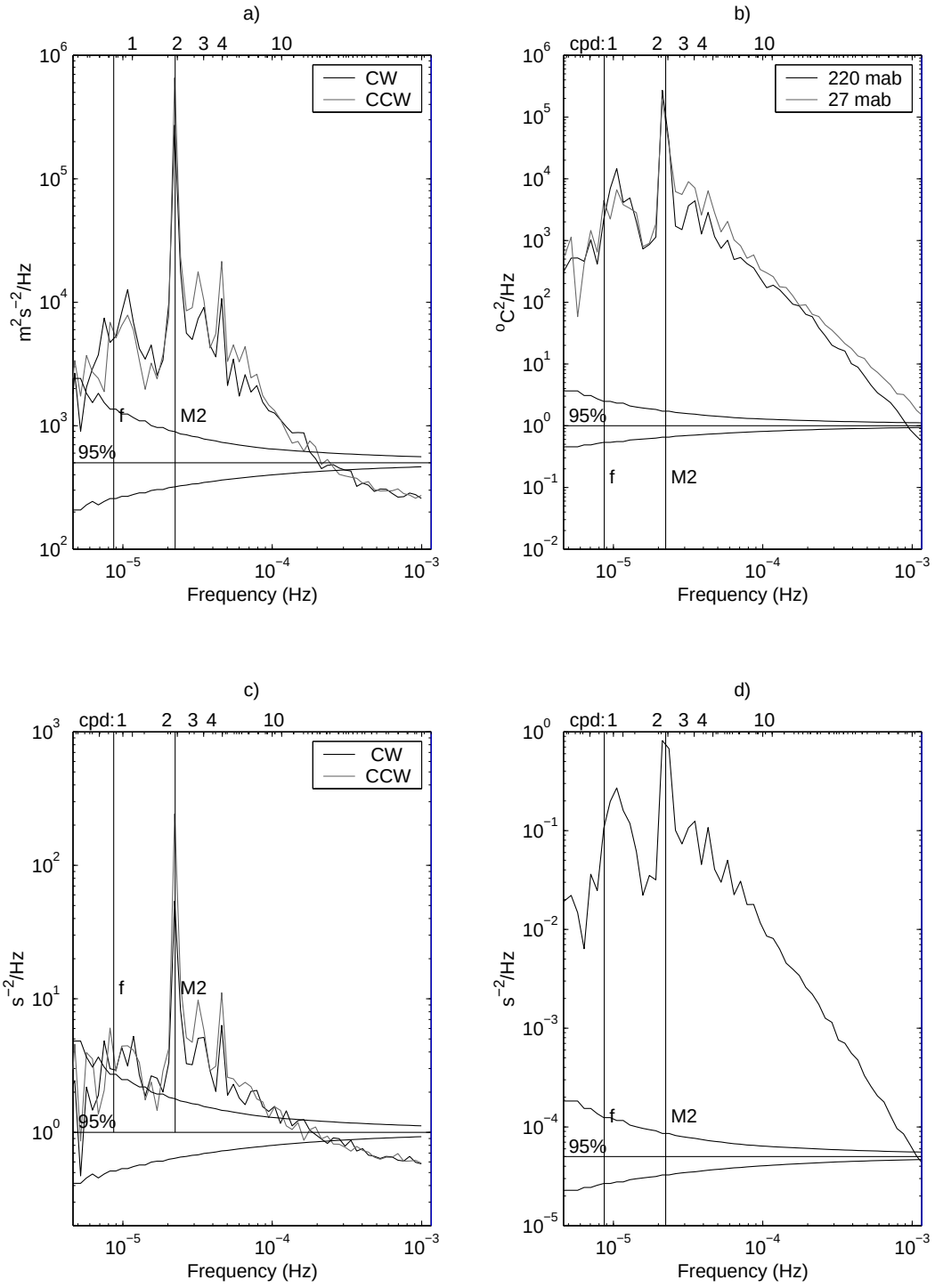

FIG. 5. Power spectra of a) horizontal current at $65mab$, b) temperature ($220mab$ and $27mab$), c) vertical shear of the horizontal current (between 40 and $65mab$), d) depth-averaged buoyancy frequency (27 to $220mab$). Top abscissa is in cycles per day (cpd).

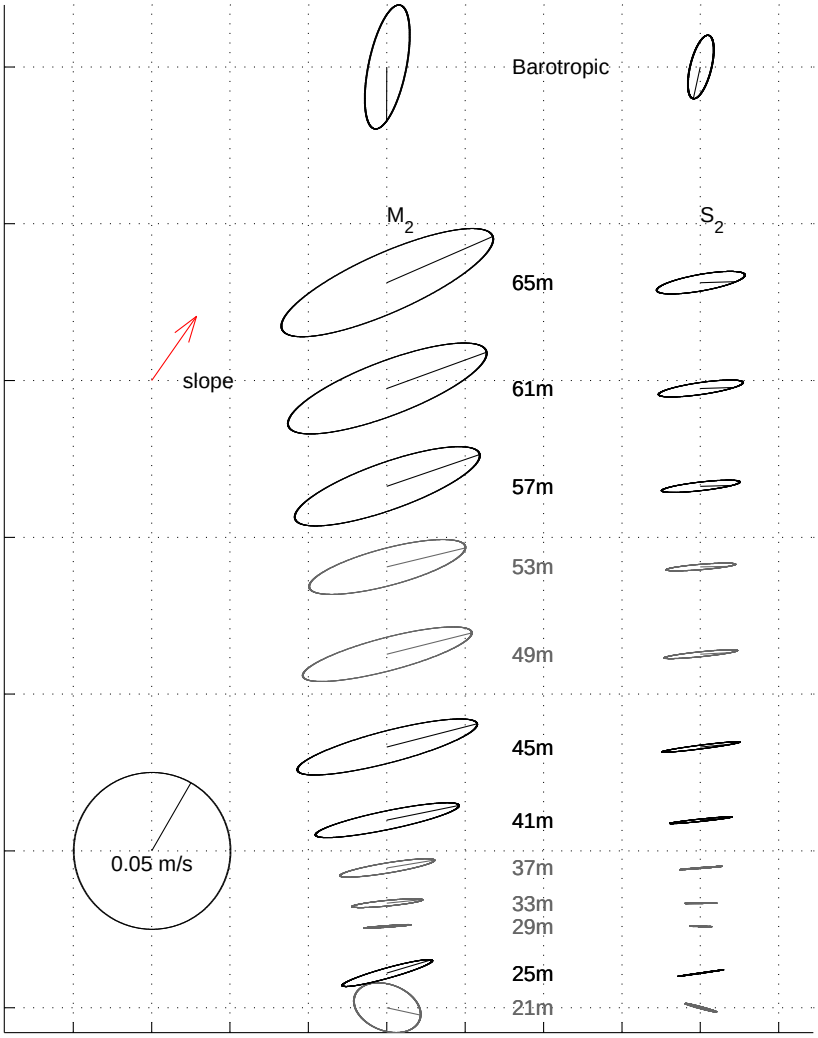

FIG. 6. The M_2 (left) and S_2 (right) measured horizontal current ellipses, with suspect depth bins in gray (i.e., side lobe contamination problems). Barotropic current ellipses predicted by the TPXO model (Egbert 1997) are depicted at the top. The direction of the topographic gradient is indicated with the gray arrow on the left.

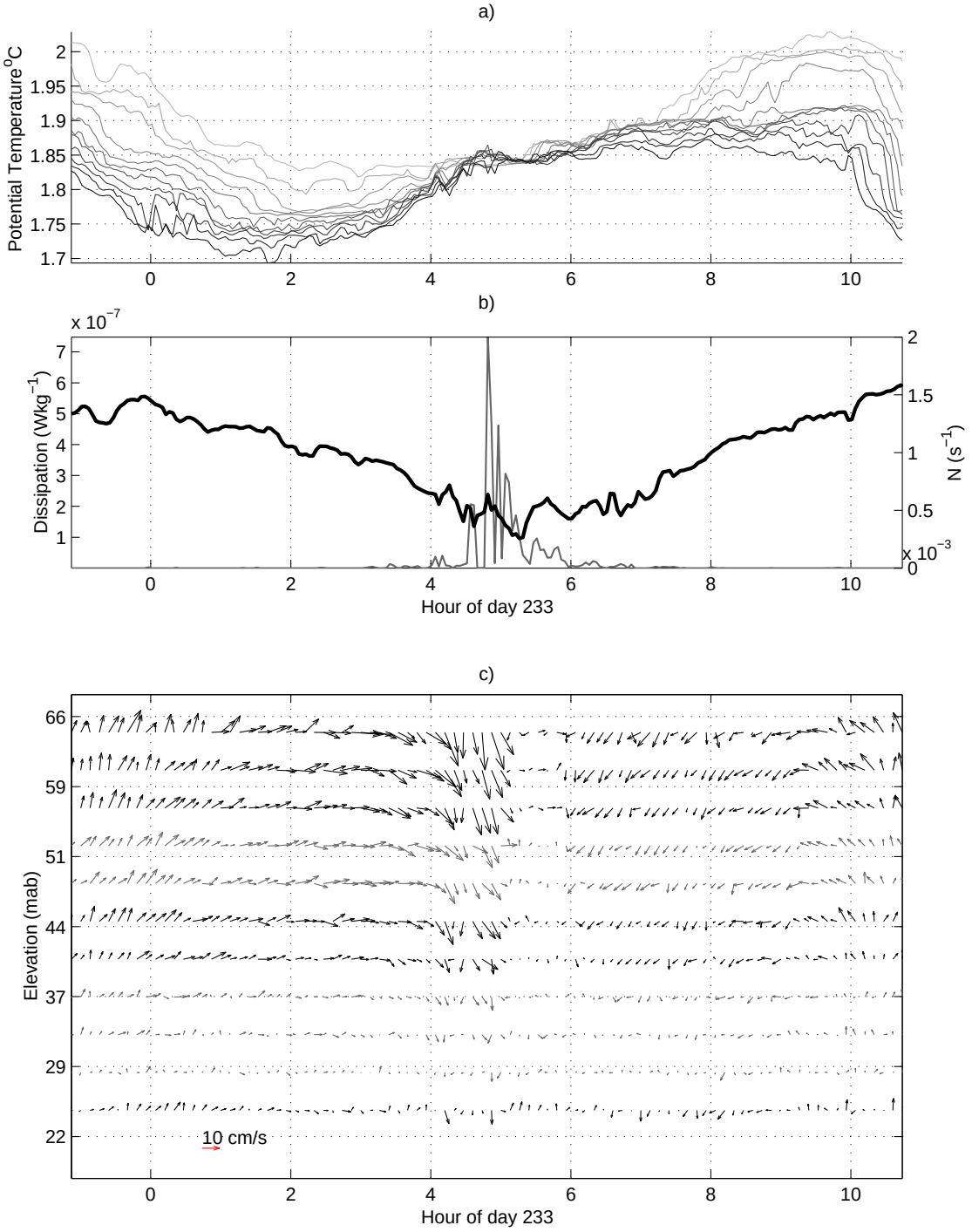

FIG. 7. A characteristic overturn event depicted in 12 hour time series (day 233) of a) potential temperature recorded at 27, 43, 59, 75, 91, 107, 124, 147, 171, 195, and 220 mab, with darker lines correpsonding to smaller elevations above the bottom, b) estimated dissipation (ϵ, equation 3, thin gray line) and depth-averaged buoyancy frequency (27 to $220mab$, thick black line), and c) horizontal currents, rotated so that across-slope velocity is vertical. Depth bins with suspect side lobe contamination are shown in gray.

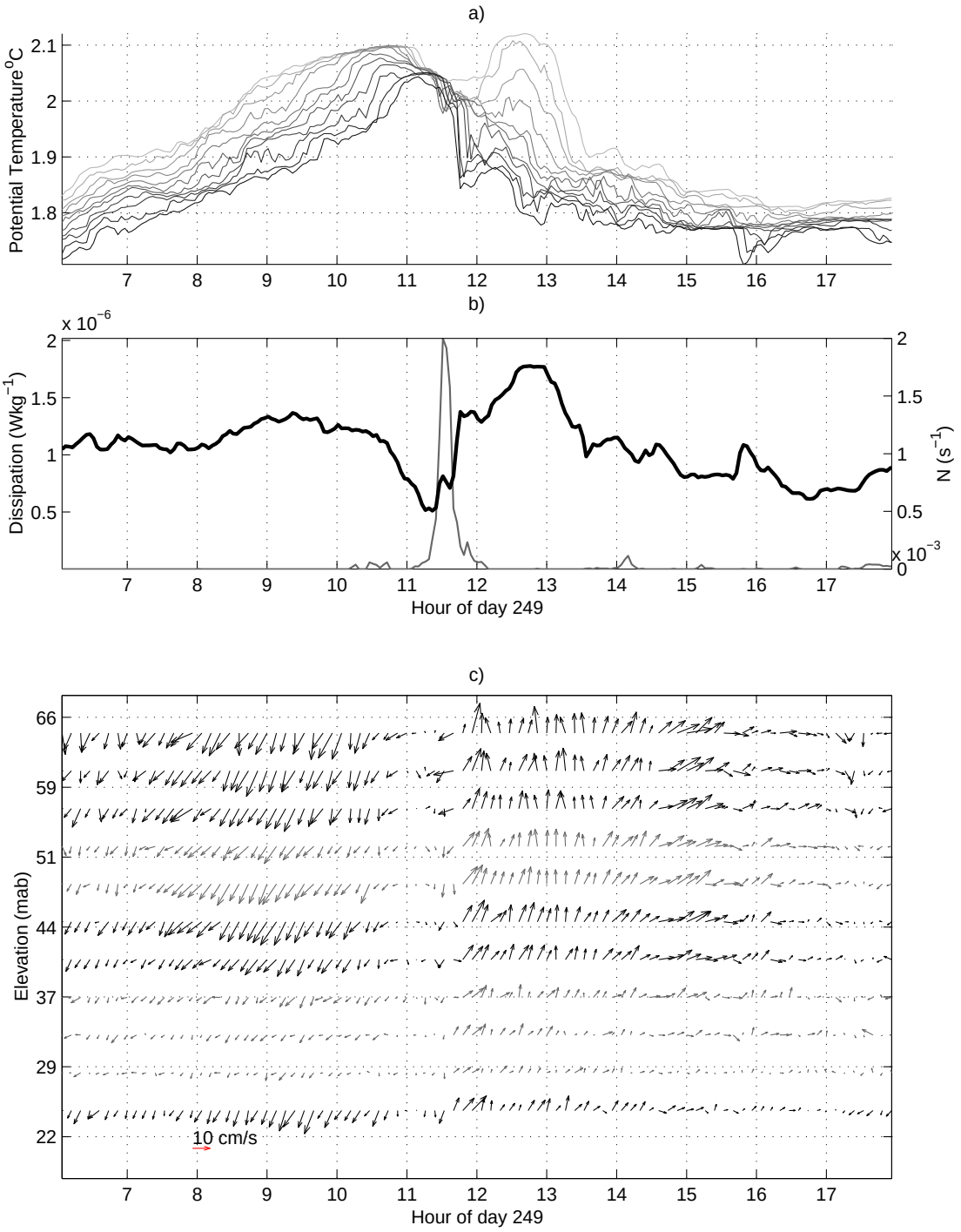

FIG. 8. Same as figure 7 for day 249, showing an overturn during a different phase of the tide.

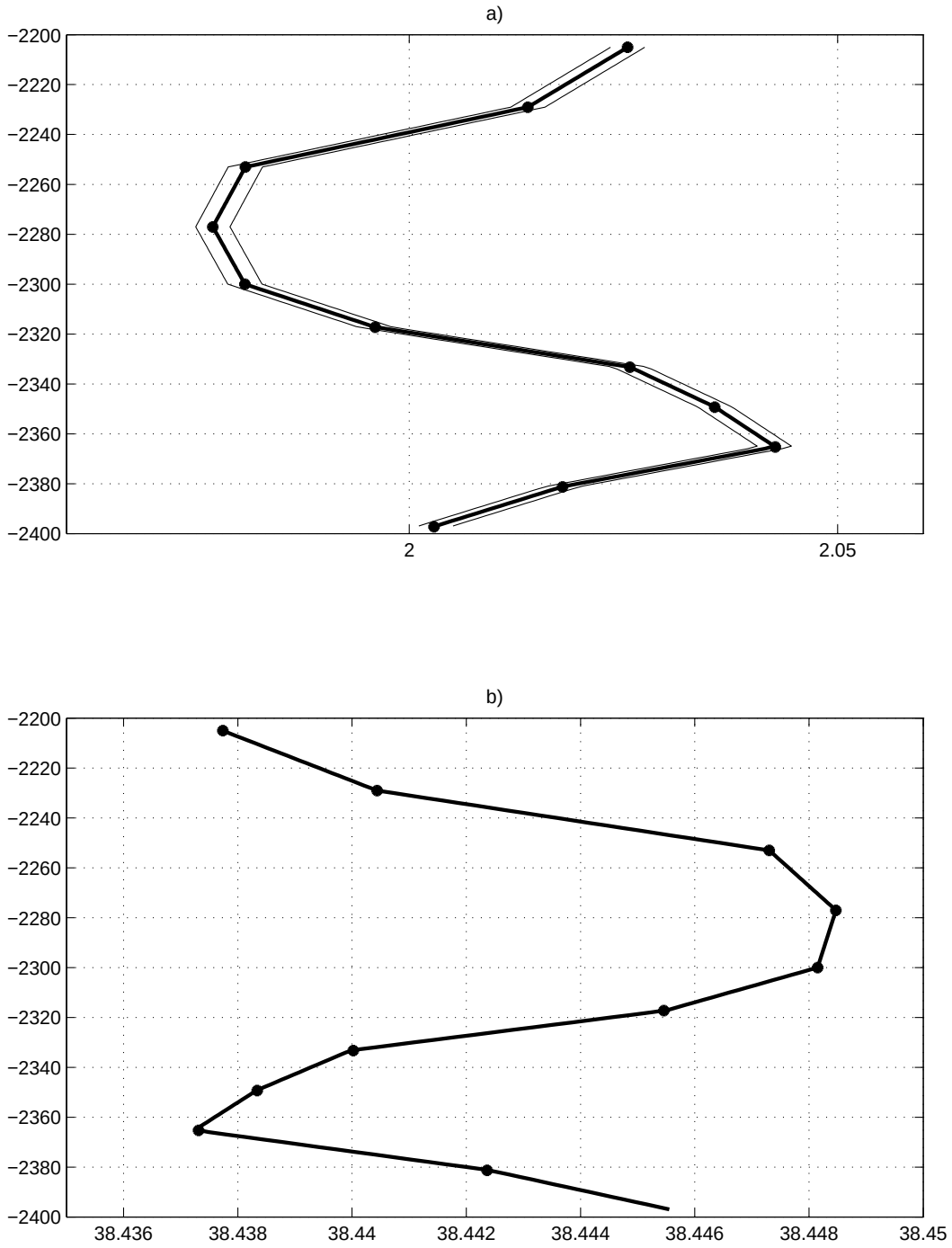

FIG. 9. a) Vertical profile at day 249, hour 11.5 (figure 8) of measured absolute temperature after removing of long term bias. '*' indicate the locations of the instruments. Thin lines represent the measurement plus or minus the nominal accuracy of the instruments. b) infered potential density ($-1000kgm^{-3}$).

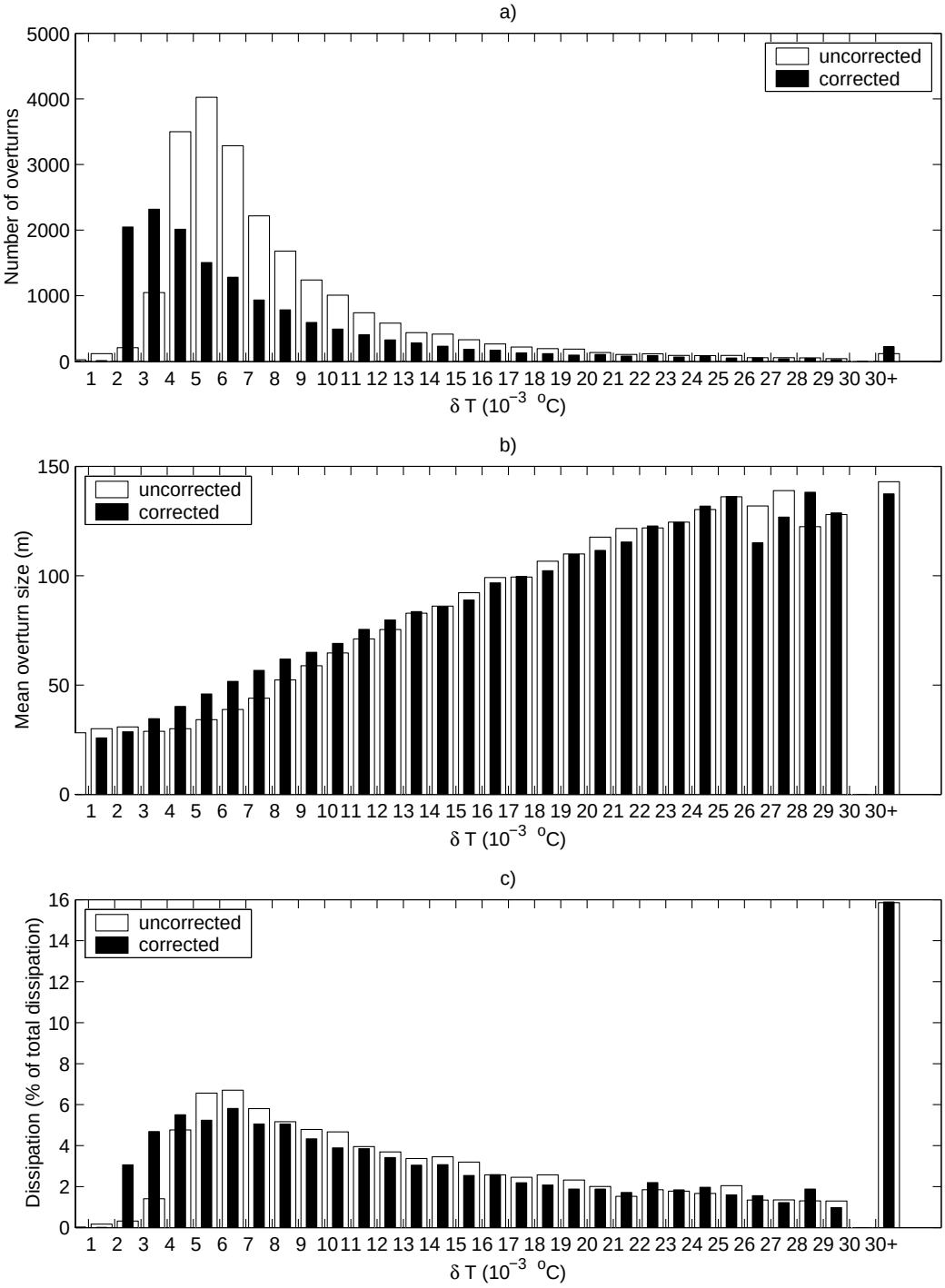

FIG. 10. a) The distribution of the number of overturns, before and after the temperature correction, as a function of the observed temperature difference across the depths of the overturn. b) The distribution of overturn size as a function of the temperature difference across the overturn. c) The distribution of the percentage of the total dissipation contributed by the overturns, as a function of the temperature difference across the overturn.

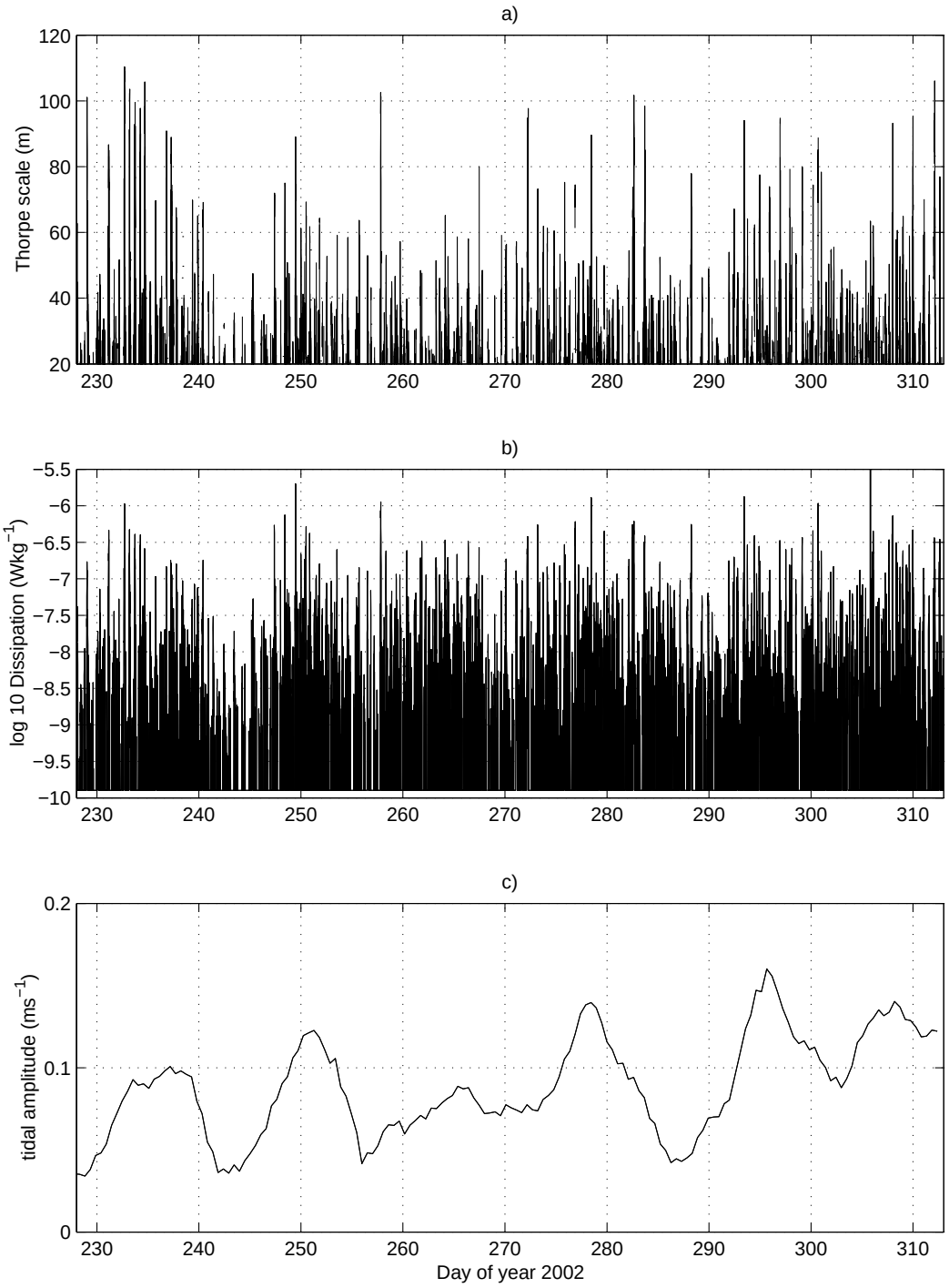

FIG. 11. a)The estimated Thorpe scale (L_T), b) dissipation (ϵ), and c) the measured semidiurnal tidal amplitude using horizontal currents at $65mab$.

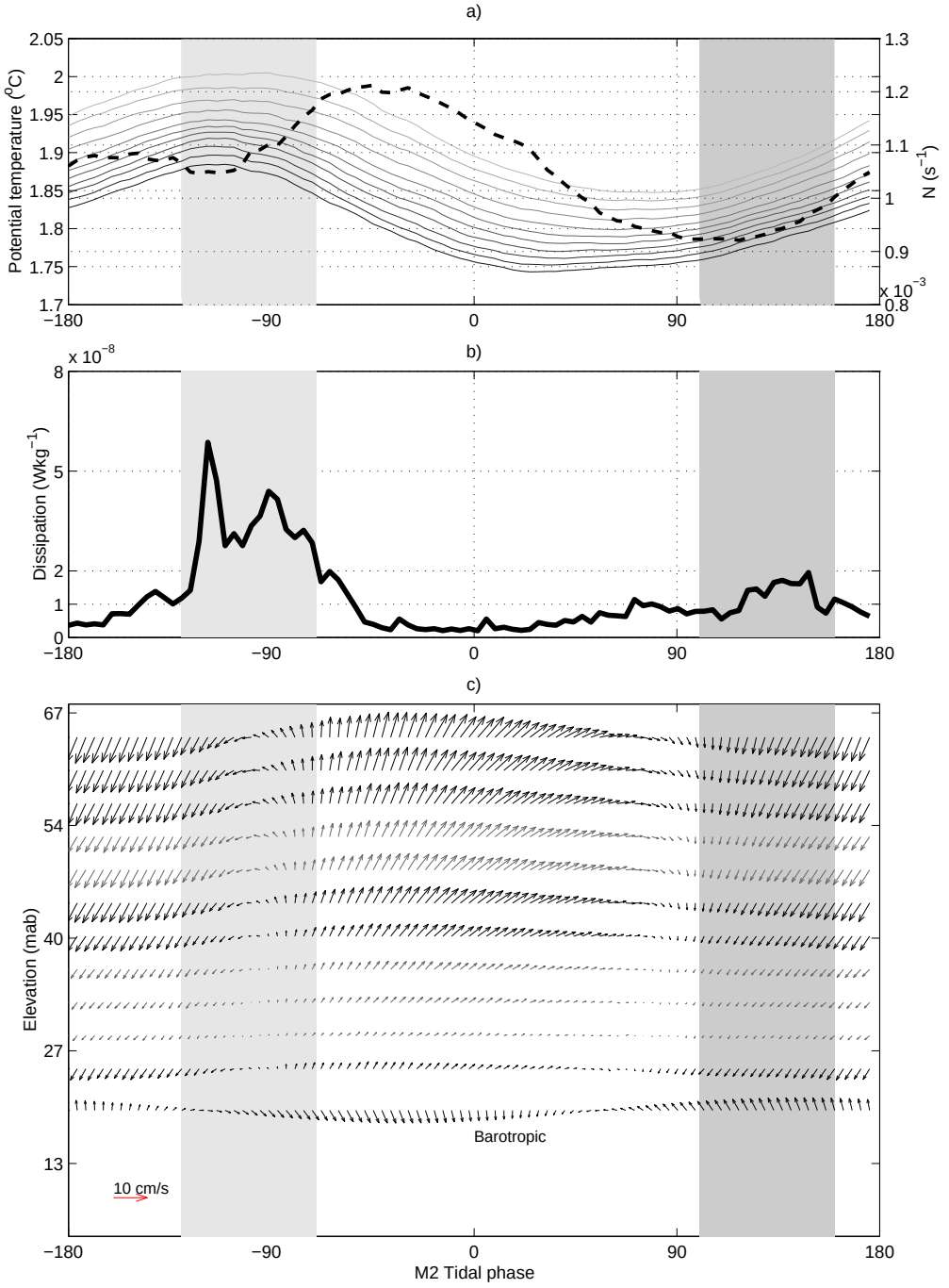

FIG. 12. A composite semidiurnal tidal cycle, obtained using ensemble phase averages over the entire time series, of a) potential temperature recorded at 27, 43, 59, 75, 91, 107, 124, 147, 171, 195, and 220 mab, with darker lines correpsonding to smaller elevations above the bottom, depth averaged buoyancy frequency (27 to 220mab, dashed black line), b) estimated dissipation (ϵ, equation 3), and c) horizontal currents, rotated so that across-slope velocity is vertical. Depth bins with suspect side lobe contamination are shown in gray. Estimates of the barotropic current (TPXO (Egbert 1997)) are included. Shaded areas indicate phases of intense mixing associated with downslope flow (dark), and flow reversal (light).

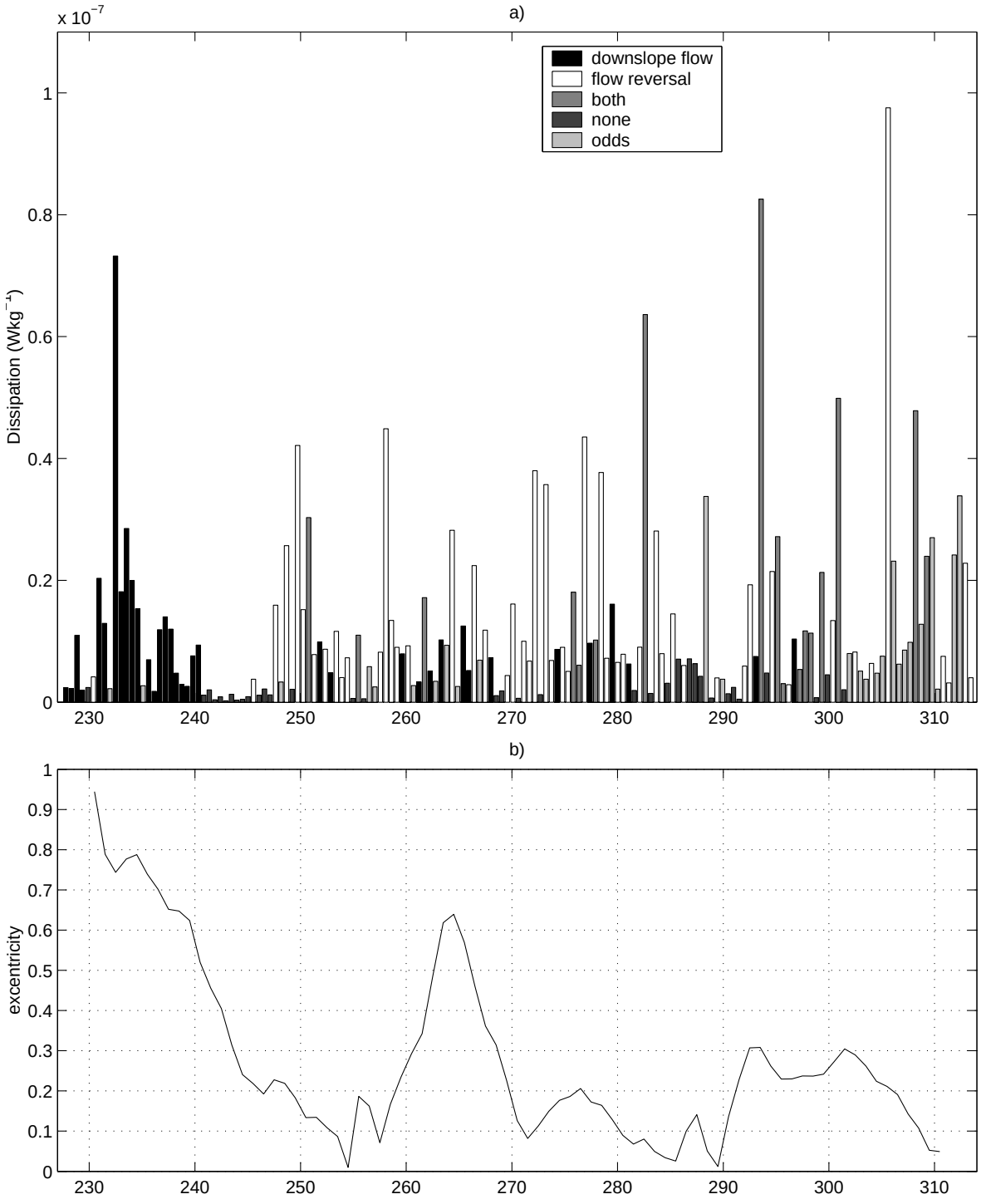

FIG. 13. a) Dissipation (ϵ), averaged over a semidiurnal cycle, is classified in terms of the dominant mixing types that occur during the cycle. b) The eccentricity of the semidiurnal current ellipse, quantified as the ratio of the minor over the major axis current amplitude. Ellipse amplitudes are obtained from a harmonic analysis of 7 days subrecords.

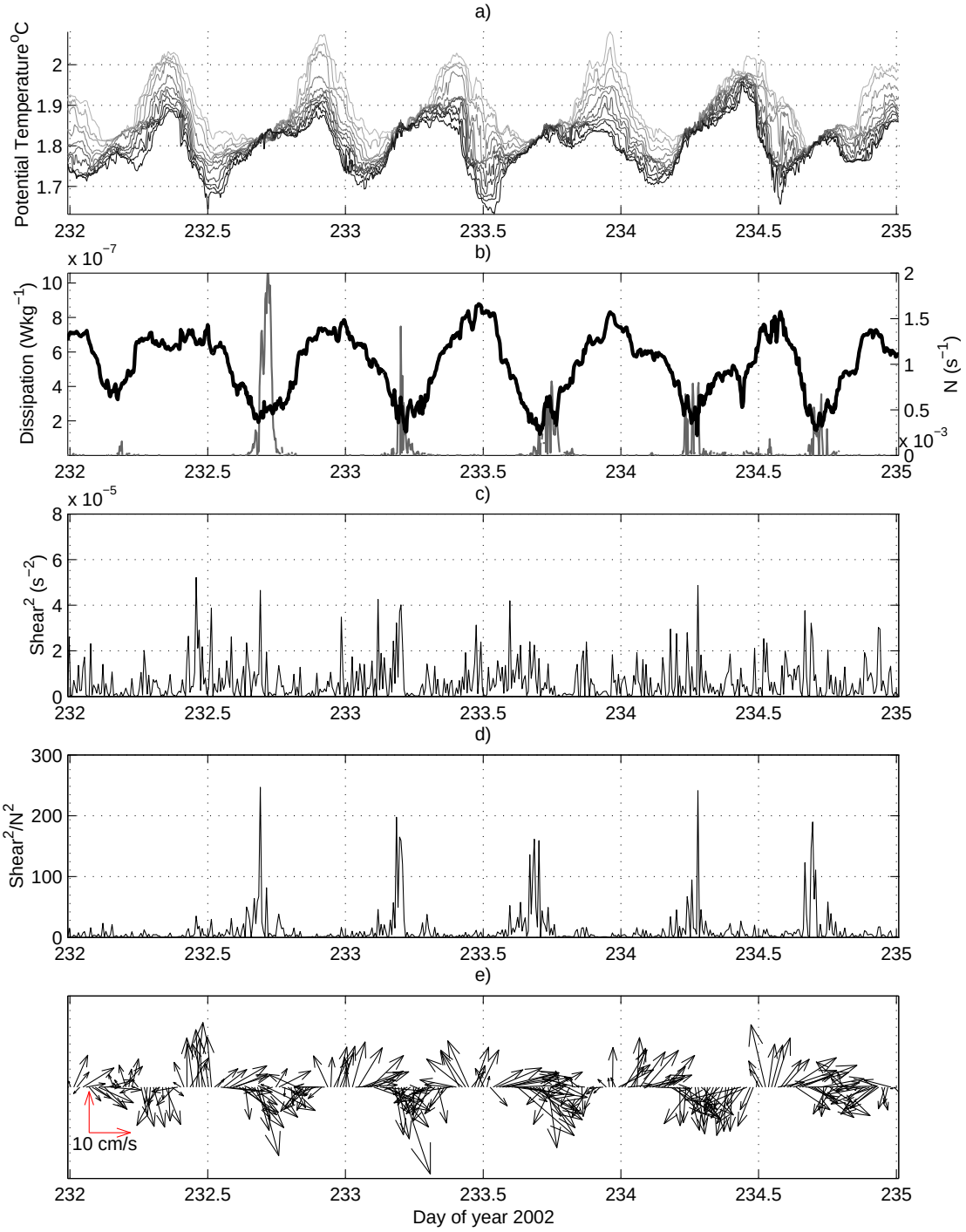

FIG. 14. Downslope flow mixing events in 3 day time series of a) potential temperature, b) depth-averaged buoyancy frequency N (27 to 220mab, thick black line), and estimated dissipation (thin gray line), c) square of the horizontal current shear (from 41 to 65mab), d) inverse Richardson number (from shear and N above), and e) the horizontal velocity (at 65mab).

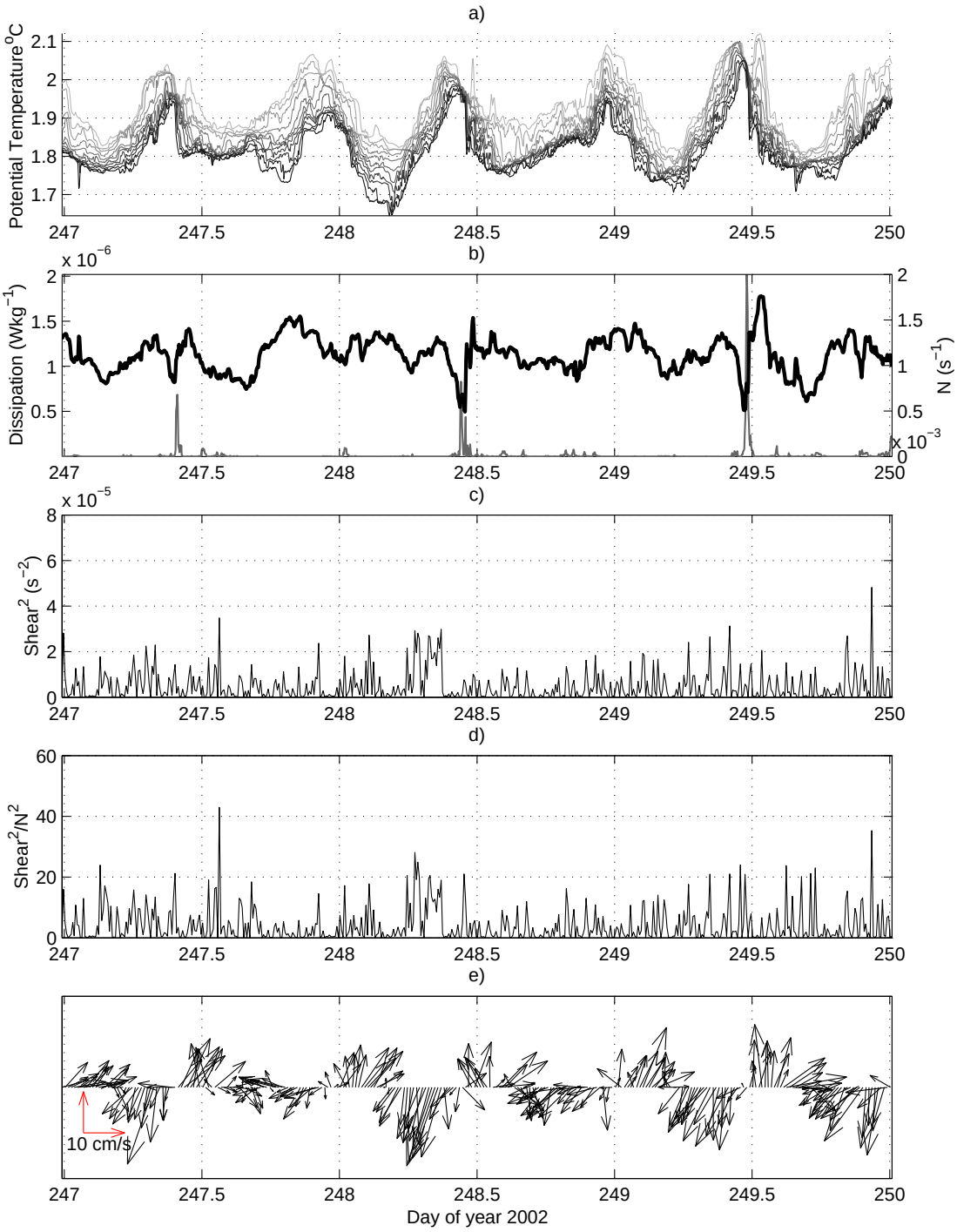

FIG. 15. Same as figure 14 for a period of flow reversal mixing events. .